Non-Newtonian flow of highly-viscous oils in hydraulic components

I.K. Karathanassis[1, *], E. Pashkovski[2], M. Heidari-Koochi[1], H. Jadidbonab[1], T. Smith[3], M. Gavaises[1], C. Bruecker[1]

[1]School of Mathematics, Computer Science and Engineering, City, University of London, EC1V 0HB London, UK
[2]The Lubrizol Corporation, Wickliffe, OH 44092, USA
[3]Lubrizol European Research and Development Centre, Nether Lane, Hazelwood, DE56 4AN Derby, UK

*Corresponding author: Ioannis.karathanassis@city.ac.uk

Abstract. Viscous oils flowing in the geometrically-complex hydraulic circuits of earth-moving machines are associated with extensive friction losses, thus reducing the fuel efficiency of the vehicles and increasing emissions. The present investigation examines the performance effectiveness of different hydraulic oils, in terms of secondary-flow suppression and pressure-drop reduction. The flow of two non-Newtonian oil compounds, containing poly(alkylmethacrylate) (PMA) and poly(ethylene-co-propylene) (OCP) polymers, respectively, have been comparatively investigated against a base, monograde liquid through Particle Image Velocimetry. An 180^o curved-tube layout and a check-valve replica have been selected as representative examples of the hydraulic components comprising the hydraulic circuit. The flow conditions prevailing in the experimental cases are characterised by Reynolds-number values in the range 76-1385. Precursor viscosity measurements with shear rate along with a theoretical analysis conducted using the FENE and PTT models have verified the influence of viscoelasticity and/or shear-thinning on the liquid flow behaviour. PIV results have demonstrated that viscoelastic effects setting in due to the OCP additives tend to reduce the magnitude of the secondary flow pattern, commonly known as a Dean-vortex system, arising in the curved geometry by as much as 15% on average compared to the base liquid. A similar flow behaviour was also demonstrated in the valve replica layout with reference to the geometry-induced coherent vortical motion in the constriction region, where a vorticity decrease up to 38% was observed for the OCP sample. On the contrary, the flow behaviour of the primarily shear-thinning PMA oil was found to be comparable to that of the base oil, hence not presenting significant flow-enhancement characteristics.

Keywords: Dean vortices, geometrical constriction, secondary-flow suppression, PIV, rheology analysis

1. Introduction

Energy losses due to friction of any kind with reference to the major industrial sectors of processes, power generation, transportation and turbomachinery correspond to an impressive 100EJ or 20% of global energy consumption [1]. Hence, the development of new materials, either solid or liquid, can have substantial benefits for the relevant industries from both economic and emissions-reduction points of view. Especially referring to hydraulic circuits either of industrial applications or primarily of vehicles, where space limitations are also more pronounced, liquid friction can lead to substantial energy-efficiency losses. In fact, it has been estimated that pumping-power losses have a major contribution in the fuel efficiency of an earth-moving machine [2]. The present study focuses on the hydraulic circuits of earth-moving machines mainly comprising valves, straight pipes and hydraulic fittings of different sorts with the most common types being curved elbows.

Single-phase flow in curved tubes has been extensively investigated both numerically and experimentally for over a century. The vast majority of research studies has focused on the flow behaviour of Newtonian liquids, in terms of the vortex system topology and dynamics arising either in the laminar or turbulent-flow regimes. It has been well established that, for laminar un-perturbed flow, a pair of counter-rotating vortices sets in even for creeping flows, occupying the entire tube-cross section. The, so called, Dean vortices, emanate from the effect of the centrifugal force on the flow field and, subsequently, the pressure gradient induced on the tube cross-section [3]. The distinct flow features of Dean flows in both regimes are summarised in [4]. Likewise, Newtonian flow through a geometrical constriction constitutes a benchmark flow-mechanics case; for instance, the well-known forward-facing step layout, where a distinct recirculation pattern arises, comprising vortices upstream and downstream the constriction location due to flow stagnation and separation, respectively [5,6].

The flow behaviour of non-Newtonian, viscoelastic fluids or dilute polymer solutions has been primarily investigated in the turbulent regime, where the presence of viscoelastic additives has been verified to lead to suppression of the flow turbulence level. Flexible additives have been found to rearrange their topology into micellar thread-like structures impeding turbulence-generating vortical motion in the wall boundary-layer region [7]. Several DNS studies concur that polymers stretch as they are entrained by the near-wall vortices and extract energy, thus dampening their motion [7–9]. Depending on the polymer relaxation time, the elastic energy stored in the viscous sub-layer can be subsequently released in the buffer and log layers; hence, drag reduction is accomplished. The effects of non-Newtonian stresses are associated with a decrease in the streamwise vorticity fluctuations in the viscous sublayer and an increase in the spacing between the streaks of low-velocity fluid in the buffer layer [10,11]. Recent experimental evidence confirms that increased elasticity effects tend to suppress benchmark streamwise vortices [12]. Impedance in the motion of the quasi-streamwise vortices, regulating the onset of turbulence, has been also associated with the increase of extensional viscosity of polymer solutions, as reported in [13]. Hence, apart from the influence of elasticity, extensional viscosity strain-thickening has also been postulated to contribute to turbulent drag reduction.

On the contrary, few studies are available in the literature focusing on laminar non-Newtonian flows. Shear-thinning liquids assumed to represent blood flow, although in reality the flow is also viscoelastic, have been investigated in curved tubes, which stand as simplified replicas for arteries under both steady and transient conditions [14,15]. With reference to industrial applications, only few experimental investigations have dealt with Non-Newtonian flow in coils and elbows. The experimental study of Jones and Davies [16] focusing on different curved-tube layouts illustrated that the departure from Poiseuille flow is delayed to higher Dean numbers (De) under the presence of viscoelastic polymers. Non-Newtonian effects were found to be considerable for $De \geq 300$ and the differences observed in the overall pressure drop values were attributed to suppression of the secondary-flow magnitude. Tsang and James [17] proposed that the dampening mechanism of the streamwise counter-rotating Dean vortices under the presence of additives is an analogue for laminar flow conditions of the turbulence-reducing effects through dissipation of near-wall quasi-streamwise vortices. In the study of Pimenta and Campos [18], different shear-thinning liquids also exhibiting certain degrees of viscoelastic behaviour were comparatively examined in a helical-coil layout under laminar flow conditions. The liquids exhibited reduced friction losses compared to Newtonian flow. Nevertheless, it was inferred by the experimental data that an increased effect of viscoelasticity hinders the extent of reduction.

Moreover, few studies examine non-Newtonian Dean flows from a numerical stand-point. Helin and Monpean [19] investigated the evolution of Dean-vortex topology of a shear thinning and viscoelastic liquid in a rectangular 180^o duct. For Dean numbers in the range 125-150, the numerical results demonstrated that either increasing the power-law index associated with the shear-thinning behaviour of the liquid or decreasing the material parameter characterizing the elongational behaviour of the Phan Thien–Tanner (PTT) model leads to retardation in the onset of a four-vortex topology. Malheiro et al.

[20] also verified that shear-thinning effects and increased fluid elasticity precipitate the onset of two vortex-pairs topology in a curved 90^o bend. Similar conclusions on the effect of elasticity with reference to the onset of instabilities and recirculation formation have also been established for polymer-solution flows in sharp 90^o bends [21–23]. Experimental and numerical studies referring to non-Newtonian flows with negligible inertial effects in serpentine channels of varying radii of curvature [24,25] have demonstrated that the onset of a cross-stream secondary flow is owed to the emerging first normal-stress differences. This instability has been characterised as the viscoelasticity-induced analogue of the Dean instability. Finally, the numerical studies of Fan et al. [26] and Norouzi et al. [27], concur that small negative values of the fluid second normal-stress difference lead to suppression of the secondary-flow pattern arising in curved geometries, whereas increasing values of the first difference have the opposite effect. The two studies followed different approaches to account for viscoelasticity, i.e. an Oldroyd-3-constant and a second-order-fluid model, respectively.

Experimental and numerical studies referring to viscoelastic flows through geometrical constrictions have been mainly focused on creeping flows, i.e. assuming negligible effects of viscous forces. Such studies are inspired by industrial processes incorporating polymer melts with high viscosity values, thus constituting the assumption of negligible Reynolds number valid. Specifically referring to creeping flows, it has been established through flow visualisation and numerical simulations that increasing the effect of elasticity leads to increase in the size and intensity of the corner vortices setting in due to flow stagnation at the location of geometrical constriction [28,29]. Nevertheless, it has been recently demonstrated by Pitz et al. [30] through simulations employing the exponential PTT model that the effect of the Weissenberg number (Wi), i.e. the effect of elasticity, is becoming ambiguous as the Reynolds number increases. Their numerical results on a two-dimensional forward-facing step for Reynolds-number values in the range $5 \cdot 10^{-4}$ up to 250 suggest that for $Re \geq 2.5$ increase of Wi leads to decrease of the vortices magnitude, while elasticity for lower Re values can also have a suppressing effect on the recirculation pattern for $Wi \geq 10.0$. It is worth to mention that shear-thinning and viscoelasticity effects for a fluid with non-zero second normal stress difference have been found to reduce the magnitude of the recirculation pattern arising downstream a contracting/expanding geometry, as demonstrated by simulations of Poole et al. [31] for laminar flow.

The referenced literature makes clear that a liquid of non-Newtonian nature can have varying effects on the onset of coherent vortical-motion depending on exact rheological properties and flow conditions. Notwithstanding this fact, experimental data on Non-newtonian flows with coherent recirculation are scarce and with no clear link to actual industrial applications. The basic aim of the present investigation is to evaluate different oil compounds in terms of flow efficiency and quantify their capability in suppresing secondary-flow motion and reducing friction losses in the hydraulic circuit of a heavy-duty machine. Two non-Newtonian liquids are comparatively examined against a reference monograde oil. The oil properties are determined beforehand through rheological measurements, while their flow behaviour is elucidated through PIV. For the needs of the present investigation, a 180^o curved-tube layout and a control-valve replica have been employed, representing typical components of hydraulic circuits.

2. Experimental methodology

The three hydraulic fluids considered in this study are formulated with the same mineral oils, commercial anti-wear additive system, and pour point depressant. They all meet the industry requirements of a hydraulic fluid specified by DIN 51524. The reference liquid is monograde and does not contain a polymeric viscosity modifier. It is thickened with a 600N mineral oil to a viscosity consistent with ISO (International Organization for Standardization) viscosity grade 46. This requires that the kinematic viscosity of the fluid measured by ASTM method D445 falls within 41.4 – 50.6 cSt. PMA liquid was thickened to the same viscosity grade using a high performance commercial

poly(alkylmethacrylate) viscosity modifier, while OCP liquid was thickened to the same viscosity grade using a high performance commercial poly(ethylene-*co*-propylene) viscosity modifier. The average molecular weight of both viscosity modifiers was < 40,000 $gmol^{-1}$ determined by size exclusion chromatography using poly(styrene) standards and tetrahydrofuran eluent. For the purposes of this study, these three formulations are considered identical with the exception of the oil-thickening component. The viscosity modifier concentration c_p in each oil compound is reported in **Table 1**. The present study comprises rheological measurements to verify the non-Newtonian nature of the additised compounds and PIV to quantify the effect on the recirculation patterns that arise in the hydraulic components due to the presence of polymers.

Basic quantities relevant to the flow conditions prevailing in the two test models are also shown in **Table 1**. It must be noted that the characteristic non-dimensional number suitable for characterising the flow conditions in curved tubes is the Dean number defined as the ratio of centrifugal over viscous forces. The magnitude and topology of the distinct secondary-flow motion arising correlates with De and feature similarity exists for flows of equal values of De. The Dean number is based on the Reynolds number and the tube geometry as follows:

$$Re = \frac{u_{ave} \cdot D}{\nu} = \frac{4\dot{V}}{(\pi D) \cdot \nu} \tag{1}$$

$$De = Re\sqrt{R/R_c} \tag{2}$$

Referring to the Reynolds number definition, u_{ave} is the flow average velocity, D is a characteristic length scale, $\dot{V}$ is the imposed volumetric flow rate and ν is the kinematic viscosity of the oil. Likewise, R and R_c in the Dean number definition correspond to the curved-tube cross-sectional radius and radius of curvature, respectively.

Table 1. Nominal transport properties of the hydraulic fluids examined and non-dimensional numbers characterising the flow conditions for the matrix of test cases.

Oil sample	c_p [%wt]	ν [cSt] @ 40°C	Q [L/min] 180° bend	Re/De 180° bend	Q [L/min] valve	Re valve
Reference	-	45.17				
PMA	9.27	49.45	5-38	174<Re<1385 79<De<631	5-20	76<Re<308
OCP	6.30	46.85				

2.1 Rheology measurements

The viscosity of polymer solutions was measured using three different instruments, in order to cover a wide range of shear rates. The uncertainty associated with viscosity measurements in the entire range of shear rates examined is 3%. A double-wall Couette cell (ARES G2, TA Instruments) was used to measure viscosities in the range 1-10^3 s^{-1}, an *hts*-VROC viscometer (Rheosense, Inc.) for the range 10^4-10^5 s^{-1} and an ultra-high shear viscometer (PCS instruments, Inc.) for the range $5 \cdot 10^5$-10^7 s^{-1}, respectively. To account for shear heating at rates higher than $5 \cdot 10^5$ s^{-1}, a temperature correction was introduced using viscosity calibration standards (Cannon standards S60 and N35). Because the high-shear viscometer can only operate at elevated temperatures, all measurements were made at 80 ^{0}C, and time-temperature

superposition (TTS) [32] was employed to obtain the viscosity curves at the liquid operating temperature (~40 ^{0}C). The values of intrinsic viscosity [η] were measured at low shear rates ($\dot{\gamma} \sim 100\ s^{-1}$) and temperature of 40 ^{0}C using a Stabinger viscometer (Anton Paar). Finally, the molecular weight of polymers was determined using triple-detection Gel Permeation Chromatography (GPC) in THF (Tetrahydrofuran).

It is essential to note that relaxation times for the non-Newtonian liquids could not be measured directly, as the elasto-capillary regime was not detected in thinning filaments of the fluids [33]. This behaviour is indicative that the plausible viscoelastic nature of either one of the PMA and OCP samples is, in any case, weak. A theoretical approach was followed instead to estimate values of the liquid relaxation time λ, also required for the calculation of the Weissenberg number $Wi = \lambda\dot{\gamma}$, as analysed in detail in section 3.1.

2.2 PIV measurements

The hydraulic flow loop that was developed for the present investigation is depicted in **Fig. 1**. The working fluid was circulated through a high-pressure gear pump at steady-state conditions for flow rates up to 38 litres per minute (lpm). The liquid temperature was monitored through type-K thermocouples inserted at the inlet/outlet manifold and adjusted with the use of a heat exchanger at temperatures close to 40 ^{o}C corresponding to matching non-dimensional numbers for the liquids examined. A three-way valve placed at the outlet of the feed pump was employed for imposing the liquid volumetric flow rate, which was monitored by a turbine flow meter. Pressure transducers having a measuring range of 0-70 bars were installed in proximity to the thermo-wells at the inlet/outlet manifolds. The temperature and pressure signals were logged through an ADC card and monitored in real time.

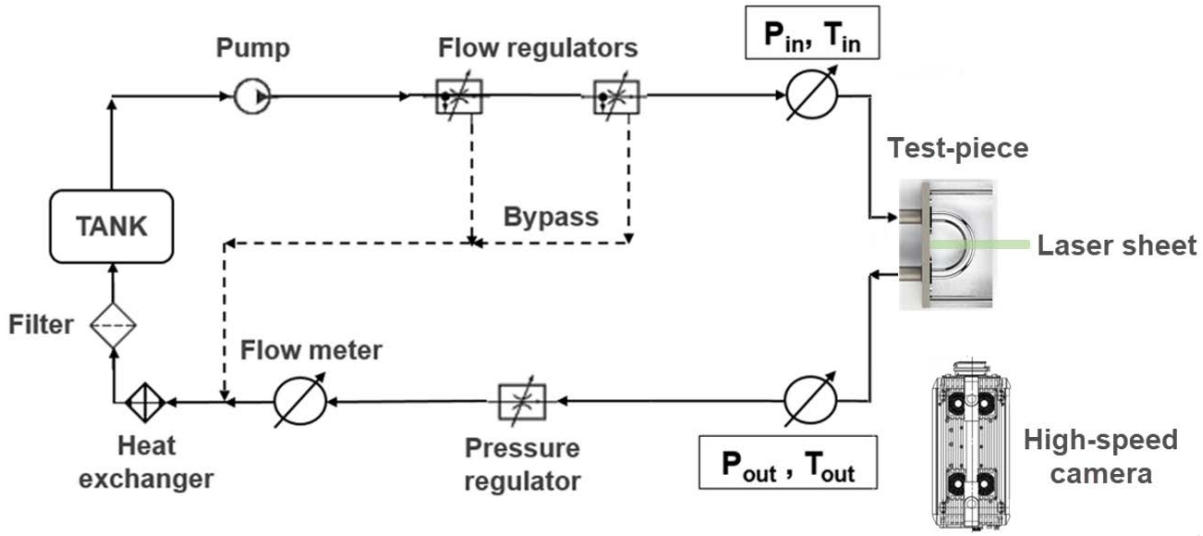

Fig. 1. Schematic of the hydraulic flow loop along with the layout of the PIV optical setup.

The optical parts incorporated in the investigation were fabricated from acrylic and their geometrical layouts corresponded to a typical 180^o bend encountered in the hydraulic system of a backhoe loader **(Fig. 2a)** and to a simplified replica of a section of the flow path inside a control valve **(Fig. 2b)**. The flow path within the valve replicated by the optical part is annotated on the left hand-side panel of **Fig. 2b**, which depicts a sliced view of the actual hydraulic device. It is evident that considerable simplifications had to be adopted to make the fabrication of the optical part feasible. Nevertheless, the internal flow-path dimensions of the replica, shown in the left panel of **Fig. 2b,** were kept similar to those of the actual device, which were obtained through laser 3-D scanning. It is also important to note that a

metallic rod has been inserted to partially block the inlet of the part inlet to replicate the asymmetrical velocity profile of the flow entering the relevant flow path in the actual device. Furthermore, the inlet partial blockage serves to induce the formation of a shear layer in the core of the downstream flow region, in order to evaluate the influence of the presence of different additives in the layer topology.

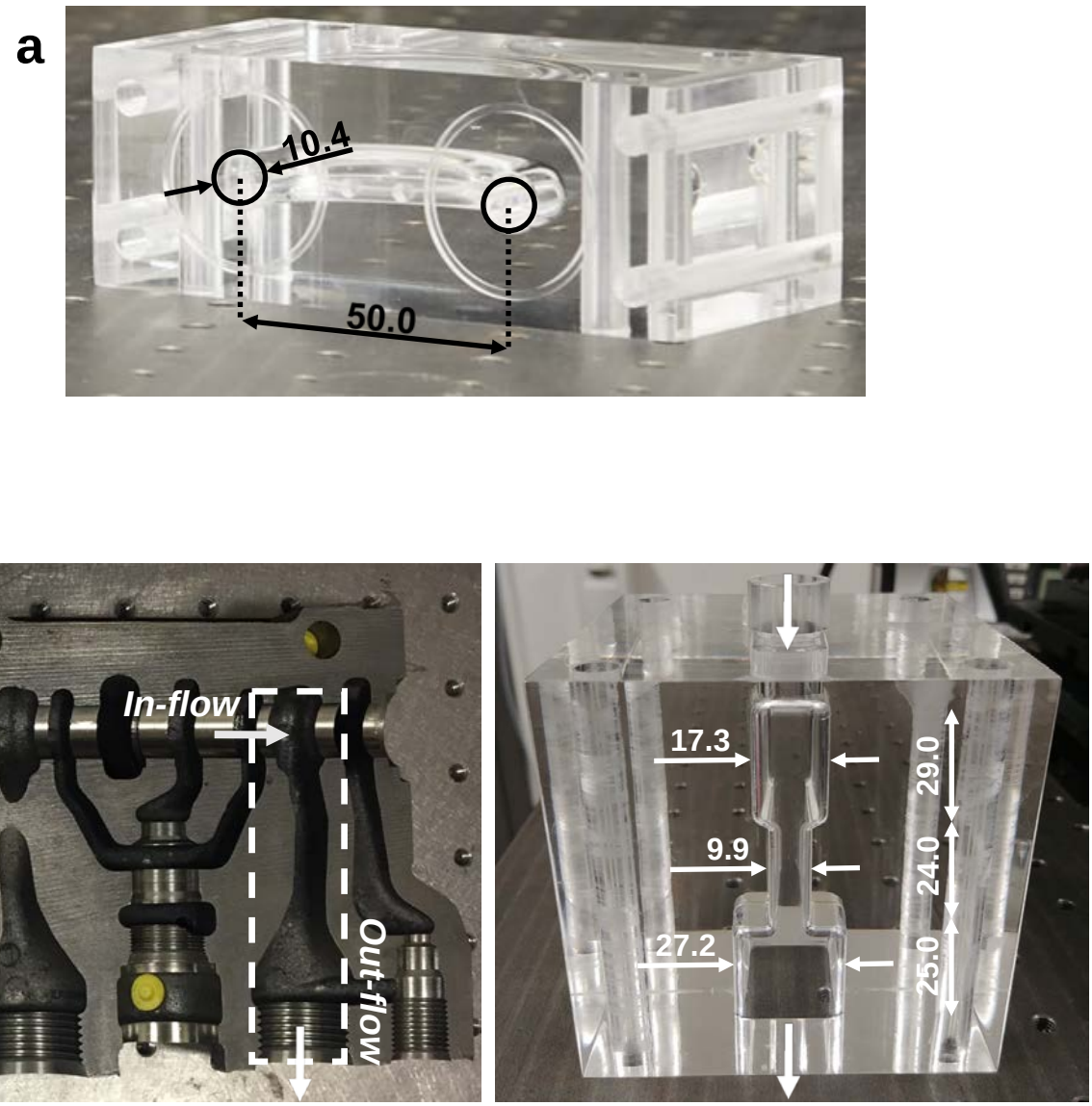

Fig. 2. Optical parts incorporated in the present study realising: (a) the 180^{o} bend and (b) the control-valve replica. A sliced view of the actual valve is also shown, along with an annotation (white rectangle) of the geometrical layout replicated, in a simplified manner, by the optical part. All dimensions in mm.

The parts were designed with flat outer surfaces to avoid laser-beam refraction due to curvature, while the refractive index of the acrylic material was matching that of organic oil (~1.48 at 25^{o}C). It was proven to be unfeasible to construct the optical part as a single solid piece through moulding, so a conventional machining process was followed instead, according to which two symmetrical parts were initially produced and subsequently diffusion-bonded to form the final geometry. Seal between the parts and manifolds was accomplished using flat rubber gaskets

Instantaneous velocity measurements were obtained through PIV in order to illustrate the recirculation magnitude in the two layouts examined. Polyamid seeding particles with a mean particle diameter of 20

μm (Dantec Dynamics) and density matching that of organic oils were used for the PIV measurements. With regard to the optical part of the test rig, a 5W laser (Dantec Dynamics RayPower) was employed to illuminate the regions of interest. The laser beam was collimated to a rectangular sheet with thickness of 2 mm. A high-speed CCD camera (Photron SAZ) was placed at a 90^o orientation with reference to the laser, so as to record the flow in the illuminated cross-section. A long-distance microscope (Infinity K2 CF-3) was fitted to the camera providing a magnification of M=4. As depicted in **Fig. 3**, the active visualisation windows comprised the tube cross-section at the curve apex/outlet (**Fig. 3a**) and the region of geometrical constriction (**Fig. 3b**), with reference to the two models. The raw image shown in **Fig. 3a** exhibits an optical distortion at the horizontal axis of symmetry. Since, the specific layout was realised by two symmetrical parts bonded together, a 'seam' formed exactly at the axis causing a slight refraction of the laser beam. During the post processing of the raw images and prior to performing the cross-correlation procedure, the image contrast was enhanced and this effect was partially alleviated. Furthermore, it has been verified that at least 20 particles were present in each interrogation window used to sample the frame. Since the final velocity vectors produced were obtained by the cross-correlation peak, i.e. the particle displacement exhibiting maximum probability, the displacement of few abnormal particles has no effect on the produced velocity field. For the valve replica layout, the overall dimensions of the active window (**Fig. 3b**) were adjusted accordingly, so that a frame rate of 30,000 fps is achievable, which was verified through preliminary visualisation tests to be adequate for capturing the secondary flow motion for all the flow conditions examined. The active visualization window in both cases was discretised by 896 x 776 pixels.

Post-processing of the raw PIV images was performed using an open-source Matlab code [34]. The code performs the cross-correlation of successive images, through a Fast Fourier Transform (FFT) with multiple passes in deforming interrogation windows. The initial pass uses relatively large interrogation areas (window size of 128 x 128 px^2) to calculate particle displacement, in order to enhance the signal-to-noise ratio. The displacement information of the first pass is used to translate and deform the interrogation areas of subsequent passes (window size of 64 x 64 px^2) in a sequential manner. Two passes have been used in total in the present investigation, with the maximum displacement being always kept below one quarter of the interrogation area to maintain the background noise levels low in the correlation matrix.

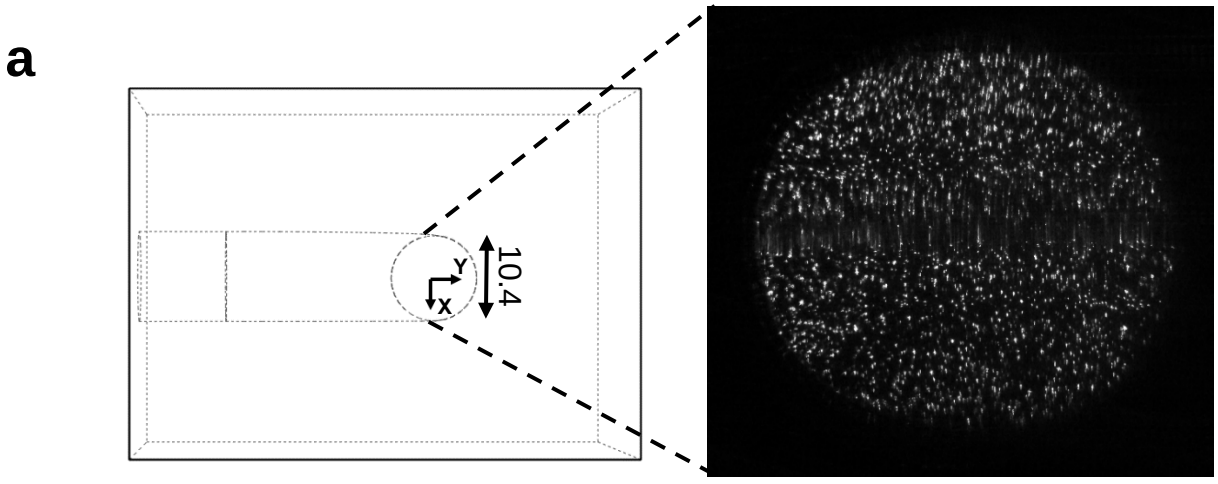

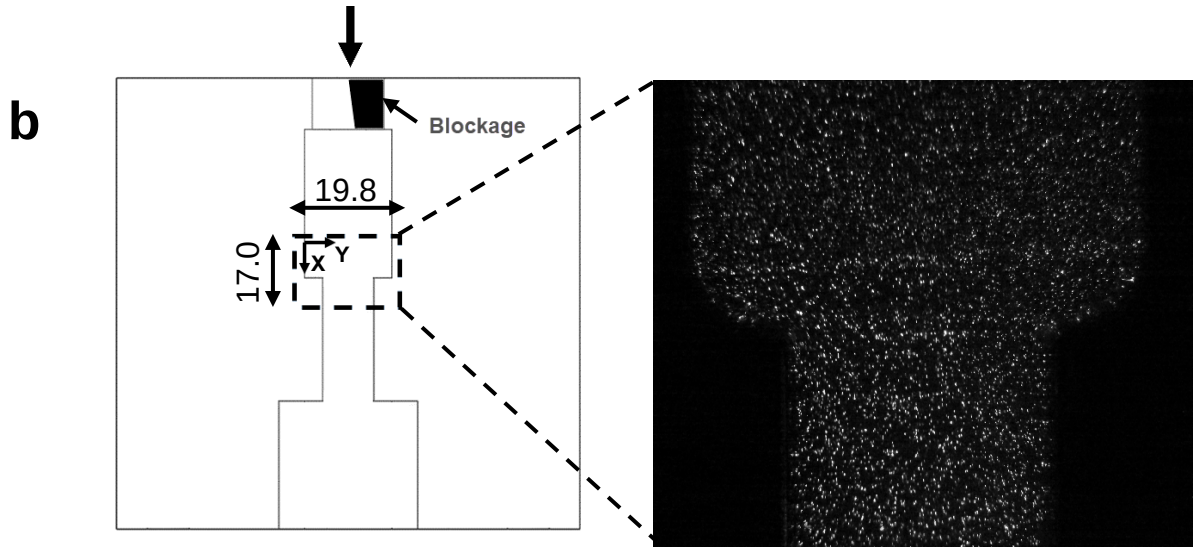

Fig. 3. Active window and indicative raw PIV images: (a) apex of the 180^o bend and (b) geometric constriction of the valve replica.

2.3 Experimental uncertainty

A typical error propagation analysis, as presented in [35], has been followed to estimate the uncertainty of non-dimensional numbers based on the accuracy of the instrumentation employed and the geometrical uncertainties. The maximum uncertainties associated with the values of the Reynolds and Dean numbers have been estimated to be approximately equal to 4%. With reference to the PIV data, the uncertainty U_u in the instantaneous velocity measurements u *(=dx/dt*) is designated by the spatial resolution of the visualisation *dx*, as it is considered that the error in the time period between successive frames *dt*, imposed by the camera frame rate, is negligible. Once again, following [35] and taking into account that the pixel size (uncertainty in *dx*) for the visualisation is equal to 13.6μm, the uncertainty in the instantaneous velocity values is estimated in the range 3.2-5.0% depending on the particle displacement between frames.

Assuming that the samples, i.e. the sets of raw images obtained are independent and follow a normal distribution of standard deviation, the uncertainty in the statistically-derived, temporally-averaged velocity is equal to:

$$U_{\bar{u}} = \frac{\sigma'_u}{\sqrt{N}} \tag{3}$$

where σ'_u is the standard deviation of the statistical sample and N is the number of samples (i.e. images) recorded. It must be noted that the standard deviation σ'_u contains the contributions of both the actual velocity fluctuations and the uncertainty in instantaneous velocity measurement U_u [36]:

$$\sigma'_u = \sqrt{\sigma^2_{u,fluct} + U^2_u} \tag{4}$$

Following the analysis presented in [36], the uncertainty associated with the instantaneous vorticity values calculated through the obtained velocity field is:

$$U_\omega = \frac{U_u}{d}\sqrt{1-\rho(2d)} \quad (5)$$

where d is the grid spacing of the interrogation window and *ρ(2d)* is the cross-correlation coefficient [37]. Two passes of the interrogation window were performed during the image post-processing with a 50% overlap at each step. The passes employed square windows of 128 and 64 pixels, respectively. Since the overlap is 50%, the grid spacing results equal to 32 pixels. The corresponding cross-correlation coefficient is related to the measurement spatial resolution and the associated uncertainty is typically not-know in an experiment. Nevertheless, it can be estimated a priori by Monte Carlo simulations for a given set of PIV processing parameters. Following [36], a value of 0.11 is assigned to ρ(2d), corresponding to an overlap factor of 50% between interrogation windows. Similar to Eq. (3), the uncertainty in the temporally-averaged vorticity is equal to:

$$U_{\bar{\omega}} = \frac{\sigma'_\omega}{\sqrt{N}} \quad (6)$$

It is important to emphasise that, since the main objective of this study is to evaluate the liquids flow performance in continuous operation within the hydraulic circuit, comparative results are presented in terms of temporally-averaged quantities (e.g. velocity and vorticity), as will be shown in the next section. The relevant uncertainties are designated by Eqs. (3) and (6) and are therefore dependent on the number of processed images. For this reason, 20,000 images have been recorded for each test case and, thus even moderate difference observed between the samples can be deemed as measurable.

3. Results and discussion

3.1 Rheological behaviour of non-Newtonian liquids

Polymer molecules can either suppress or enhance vortical motion, depending on their molecular characteristics. As has been already mentioned, a negative value of the liquid second normal-stress difference $N_2 = \tau_{22} - \tau_{33}$ can supress secondary-flow intensity [26,27]. For solutions of linear polymer molecules, the absolute value of N_2 is much lower compared to that of the first normal stress difference N_1 ($N_1 = \tau_{11} - \tau_{22} > 0$). The values of N_1 and N_2 strongly depend on shear rate $\dot{\gamma}$, i.e. $N_1 \equiv \Psi_1\dot{\gamma}^2$ and $N_2 \equiv \Psi_2\dot{\gamma}^2$, where Ψ_1 and Ψ_2 are first and second normal stress coefficients, respectively. For the low molecular-weight polymer solutions discussed in this paper, the value of N_1 cannot be measured due to insufficient sensitivity of commercial rheometers. However, it can be estimated from constitutive equations using available viscosity or shear stress data. For flexible polymer chains, the FENE (finite extensibility non-linear elastic) dumbbell model [38,39] can be used to estimate the polymer contribution to the solution viscosity as follows:

$$\eta_p = 2nk_BT\frac{b}{\dot{\gamma}(b+2)}\sqrt{\frac{b+5}{6}}\,sinh\left\{\frac{1}{3}arcsinh\left[3\dot{\gamma}\lambda_H\frac{b+2}{2(b+5)}\sqrt{\frac{6}{b+5}}\right]\right\} \quad (7)$$

where k_B is the Boltzmann constant, T is the absolute temperature, while the dumbbell relaxation time is:

$$\lambda_H = \frac{b+5}{b}\frac{[\eta]\eta_s M_w}{RT} \quad (8)$$

The dumbbell relaxation time λ_H depends on polymer intrinsic viscosity $[\eta]$, solvent viscosity η_s and the extensibility parameter b, which can be calculated through the following correlation:

$$b = 3\left[\frac{j(sin\theta/2)^2 M_w}{C_\infty M_u}\right]^{2(1-\nu)} \quad (9)$$

where $\theta = 109.5^0$ is the bond angle, $j = 2$ is the number of bonds per repeat unit, C_∞ is the characteristic polymer ratio and M_u is the molecular weight of monomer unit. The parameters required for the determination of η_p through the FENE model are summarised in **Table 2**. The definition of λ_H in Eq. (8) is given for an elastic dumbbell model, which is valid for flexible chains. The finite extensibility parameter can also be expressed as $b = \frac{L^2}{<R^2>_0}$, where L is the length of the fully extended chain and $< R^2 >_0 = N_K^{2\nu} b_K^2$ the average end-to-end distance for chains at equilibrium. Here, N_K and b_K are the number and length of the Kuhn segment, and ν is the excluded volume exponent. Especially considering theta solvents, the relation between extensibility and Kuhn-segment number reduces to $b=3N_K$. For the PMA polymer, the values of C_∞ and M_u are greater than the respective for OCP, which results in smaller extensibility of chains and smaller number of Kuhn segments per chain (see **Table 2**). In other words, the OCP polymers form flexible chains of small diameter with respect to their overall contour length and can exist in a coiled state at rest. On the contrary, PMA chains have long side-chains that are plausible to prevent coiling.

Table 2. Parameters required for the calculation of η_p through the FENE model, Eq. (7).

Sample	M_w [g/mol]	C_∞	[η] [mPa s]	η_s [mPa s]	λ_H [μs]	M_u [g/mol]	b	N_K
OCP	8700	6.74	0.193	17.97	1.2	34.65	149.2	49.7
PMA	39900	13.26	0.069	21.81	2.5	232.78	51.7	17.3

Since the FENE model *a priori* assumes $\Psi_2 = 0$, the modified Phan-Tien Tanner (PTT) [31] model can be used to estimate the Ψ_2/Ψ_1 ratio:

$$\frac{\Psi_2}{\Psi_1} = -\frac{\xi}{2} \quad (10)$$

where ξ is a material parameter, commonly referred to as non-affinity parameter. This parameter is included in the expression for polymer contribution to viscosity in the PTT model [31,40]:

$$\eta_p = (\eta_{p,0} - \eta_{p,\infty}) \frac{1+\xi(2-\xi)\lambda^p \dot{\gamma}^p}{(1+\Gamma^p \dot{\gamma}^p)^{(1-n)/p}} + \eta_{p,\infty} \quad (11)$$

where Γ is a time constant (taken approximately equal to the polymer solution relaxation time, i.e., following [40], $\Gamma \equiv \lambda$), n is the power-law index, $p > 1$, ξ is the non-affinity parameter also evident on **Eq. (10)** and $\eta_{p,\infty}$ is the polymer contribution at ultra-high shear rate. **Table 3** summarises the values of the parameters required by the formulation of the PTT model to estimate η_p; it must be noted that, as the parameters in Eq. (11) are interdependent, it was necessary to constrain some of their values.

Table 3. Parameters required for the calculation of η_p through the PTT model, Eq. (11). The following parameters are constrained as follows: ξ=0.02, $\Gamma(\equiv\lambda)=\lambda_H$, p=1.98 and n=0.

Sample	$\eta_{p,0}$ [mPa s]	$\eta_{p,\infty}$ [mPa s]	Γ [μs]	p	n	ξ
OCP	19.13 ±0.07	10.94±0.40	1.2	1.98	0	0.02
PMA	20.56±0.07	13.80±0.24	2.5	1.98	0	0.02

Eqs. (7) and (11) can be used to compare experimental data with prediction of the FENE and PTT models for the two polymers. The addition of a polymer to a base liquid leads to a shear dependence of the sample apparent viscosity. Viscoelastic fluids are typically shear thinning, i.e. their shear viscosity reduces with shear rate. Shear-thinning effects become significant for shear rates $\dot{\gamma} \geq \lambda_H^{-1}$ or $Wi \equiv \dot{\gamma}\lambda_H \geq 1$. Note that the FENE model is based on the concept of entropic elasticity that is valid for long, flexible polymer chains having large number of Kuhn segments. In **Fig. 4a**, the FENE model adequately describes the viscosity variation of the OCP solution. In other words, the number of Kuhn segments N_K~50 is sufficient for OCP chains to be approximated by the elastic dumbbells. In contrast, the viscosity of the PMA solution calculated using the FENE model is significantly lower than the experimental data (**Fig. 4b**). Hence, the assumption that Eq. (7) can also be applied to PMA chains is doubtful and furthermore the longer λ_H for PMA predicted using Eq. (8) is not deemed as accurate.

The PTT-model formulation is more sophisticated compared to that of FENE, as it is capable of predicting $N_2 \neq 0$. Therefore, the incorporation of this model in the present analysis is primarily required for a theoretical estimation of the N_2 values for the OCP sample, which cannot be directly measured. As also made clear by **Fig. 4**, viscosity variation for both samples can be described by the PTT model. According to the model formulation [40], the affinity parameter ξ is used in the reduction of the stress tensor components. Hence, even in the case that the diagonal components of the stress tensor are negligible, the shear-thinning behaviour will still be described. Nevertheless, shear thinning does not necessarily require stretching of the polymer chains and can be observed in suspensions of rigid molecules due to orientation by the flow [38]. It is also essential to underline that the parameter ξ was fixed to the maximum value of 0.02 for which Eq. (11) provided an accurate fit to the experimental data of **Fig. 4**, as for larger values considerable deviations were noted. For the specific value of ξ, the ratio of Ψ_2/Ψ_1 yields a value of -0.01 which is comparable to the value reported in [41] for flexible polymer chains. FENE model, on the other hand, assumes that the shear thinning is related to the chain stretching as the relaxation time depends on the spring constant [38]. The fact that the PTT model can adequately describe shear stress for both polymers, but FENE works only for one of them should be therefore attributed to the fundamental assumptions of their respective mathematical formulations.

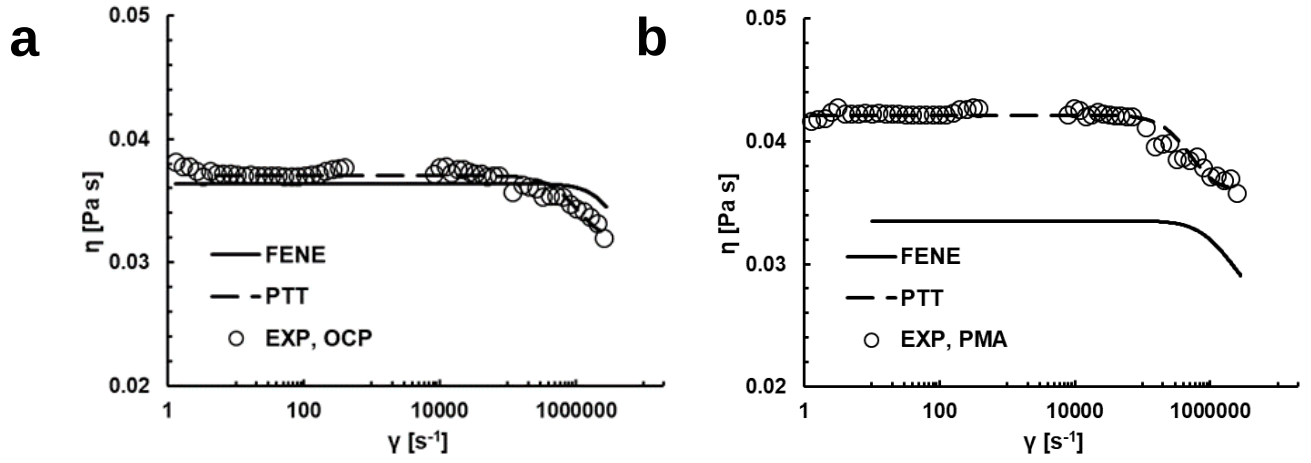

Fig. 4. Viscosity variation of the two non-Newtonian liquids with shear rate: (a) OCP and (b) PMA. Solid curves were obtained using Eq. (7) for FENE dumbbells, while dashed curves represent fits to the PTT model, Eq. (11).

FENE model formulation comprises two equations referring to the calculation of the shear stress and N1, respectively. Since FENE fails to predict the viscosity variation of PMA, subsequently it cannot be

used for the estimation of N_1 for the specific solution. Nevertheless, for the OCP solution, the value of N_1 can be calculated employing the FENE model, as follows:

$$N_1 = 4nk_BT\frac{b(b+5)}{3(b+2)}\left(sinh\left\{\frac{1}{3}arcsinh\left[3\dot{\gamma}\lambda_H\frac{b+2}{2(b+5)}\sqrt{\frac{6}{b+5}}\right]\right\}\right)^2 \quad (12)$$

where $n = c_pN_A/M_w$ is number density of polymer chains, with c_p being the polymer concentration and N_A is the Avogadro number.

The FENE-predicted N_1 distribution with shear rate for the OCP polymer is depicted in **Fig. 5**. The polymer shear stress was also calculated and depicted in the same graph. The experimental values of τ_p (circles in **Fig. 5**) were determined by subtracting the solvent contribution $\eta_s\dot{\gamma}$ from the shear-stress $(\eta_s+\eta_p)\dot{\gamma}$ values obtained experimentally. The fact that τ_p is accurately predicted by FENE acts as a validation for the calculated N_1 values, as well. Subsequently, an estimate of the value of the second normal-stress difference $N_2 \cong -0.01N_1$, which affect the secondary-flow topology as discussed in the following sections, can be provided.

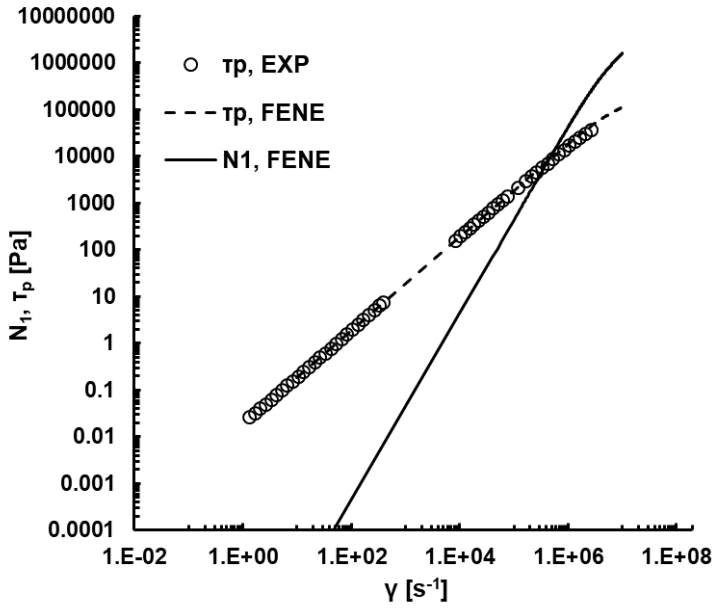

Fig. 5. Shear and normal stress difference variation with shear rate for the OCP sample. Points correspond to experimental data, while lines denote values calculated using the FENE model.

3.2 Secondary-flow topology in the examined geometrical layouts

The time-averaged secondary-flow pattern prevailing at the apex of the 180° bend for the flow conditions examined is depicted in **Fig. 6**. It must be emphasised that for the specific degree of curvature, the maximum secondary flow magnitude is expected to be reached in the vicinity of the curve apex [42]. For brevity, only the relevant plots for the reference liquid are depicted, since a qualitatively similar recirculation pattern was obtained for the additised samples as well, nevertheless with quantitative differences, which are highlighted in the subsequent figure. As depicted in **Fig. 6a**, for the lowest value of the Dean number examined, De=79, a typical two-vortex pattern is evident with the vortices exhibiting a kidney-shaped form. As the Dean-number value increases, **Figs. 6b** and **6c**, the topology of the

prevailing Dean vortices (DV) becomes more distorted and the locations of vorticity maximum are further shifted towards the inner wall of the bend. Besides, a second pair of counter-rotating vortices (SV) sets in at the tube core. It has been well established in the literature that above a critical Dean-number, designated by inherent instabilities of the flow system, the recirculation topology switches to a four-vortex system, the existence of which is attributed to the interaction of the primary Dean-vortex filaments, causing a secondary vortex roll-up [3]. For instance, experimental investigations referring to different applications have verified a four-vortex system for moderate De values in the range 100-500 [43,44]. Additional separation regions, due to the flow motion towards the tube core, appear at the bend inner wall with the lower one being more profound. **Figs. 6b-c** make evident that the recirculation pattern does not appear symmetric to the tube centre-plane. It must be taken into account that due to the high-viscosity of the examined liquids, the reported Dean-number values correspond to high flow rates reaching up to the pump-delivery limit (38 lpm), therefore induced vibrations and flow-rate fluctuations during operation are plausible to induce flow perturbations causing breakage of symmetry. Additional contributing factors constitute the geometrical quality of the part itself, as the cross section is not perfectly circular due to warping during diffusion bonding, and the manifold/optical part assembly quality.

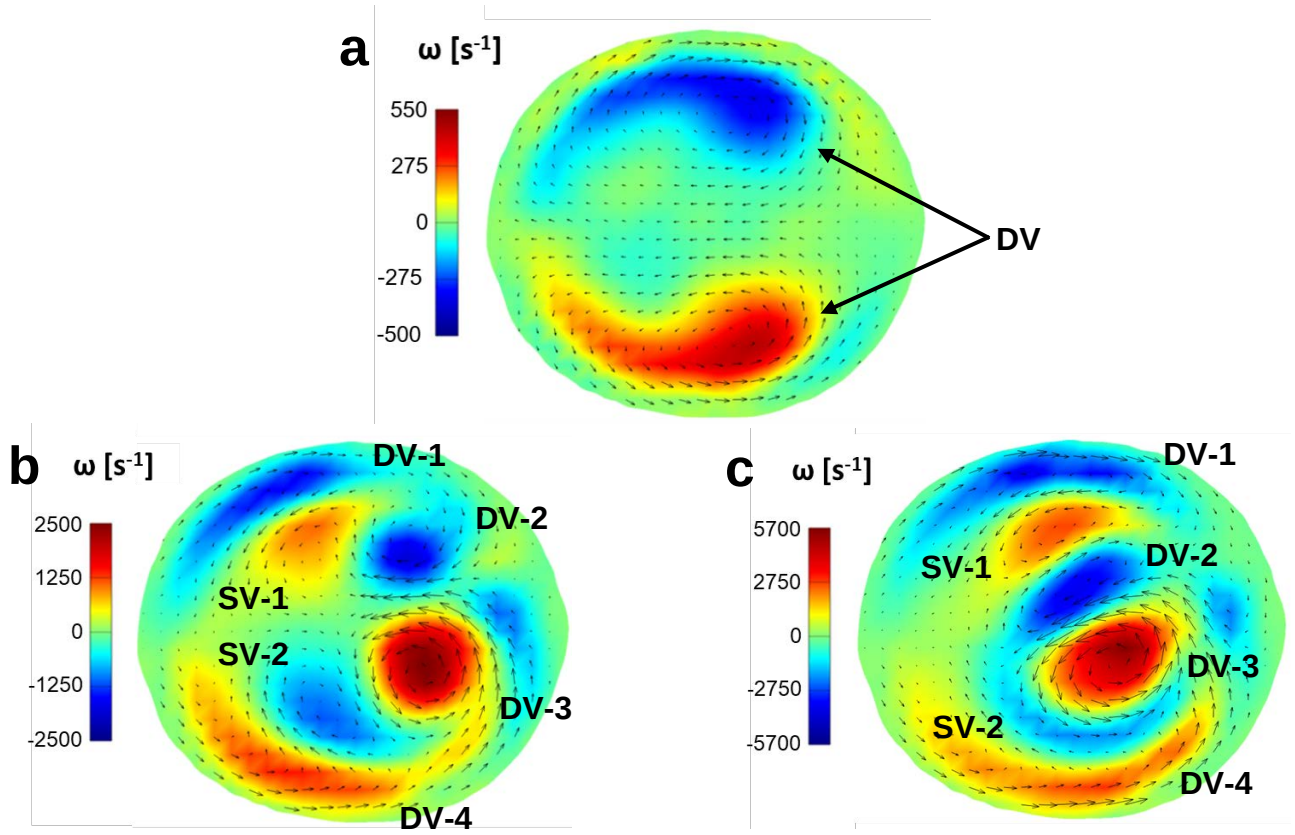

Fig. 6. Velocity vectors over vorticity contour plots depicting the time-averaged secondary-flow field and highlighting the distinct vortical structures (SV and DV) arising at the apex of the 180° bend (reference liquid): (a) Re=174/De=79, (b) Re=716/De=326 and (c) Re=1385/De=631. The experimental uncertainty $\boldsymbol{U_{\bar{\omega}}}$ associated with the temporally averaged vorticity values lies in the range 0.6 -1.0% with the largest value associated to the low Dean-number(=79) case.

Fig. 7 depicting successive instantaneous time instances of the velocity field for De=631 (**Fig. 7a)**, along with the respective velocity-magnitude mean and standard-deviation images (**Fig. 7b**) verify that a time-invariant secondary flow pattern arises in the curved tube even for the highest flow rate examined. The prevailing lower Dean vortex remains static and larger in size compared to the respective upper one.

Hence, the averaged flow field provides a straightforward representation of the intensity of the vortical structures arising in the bend.

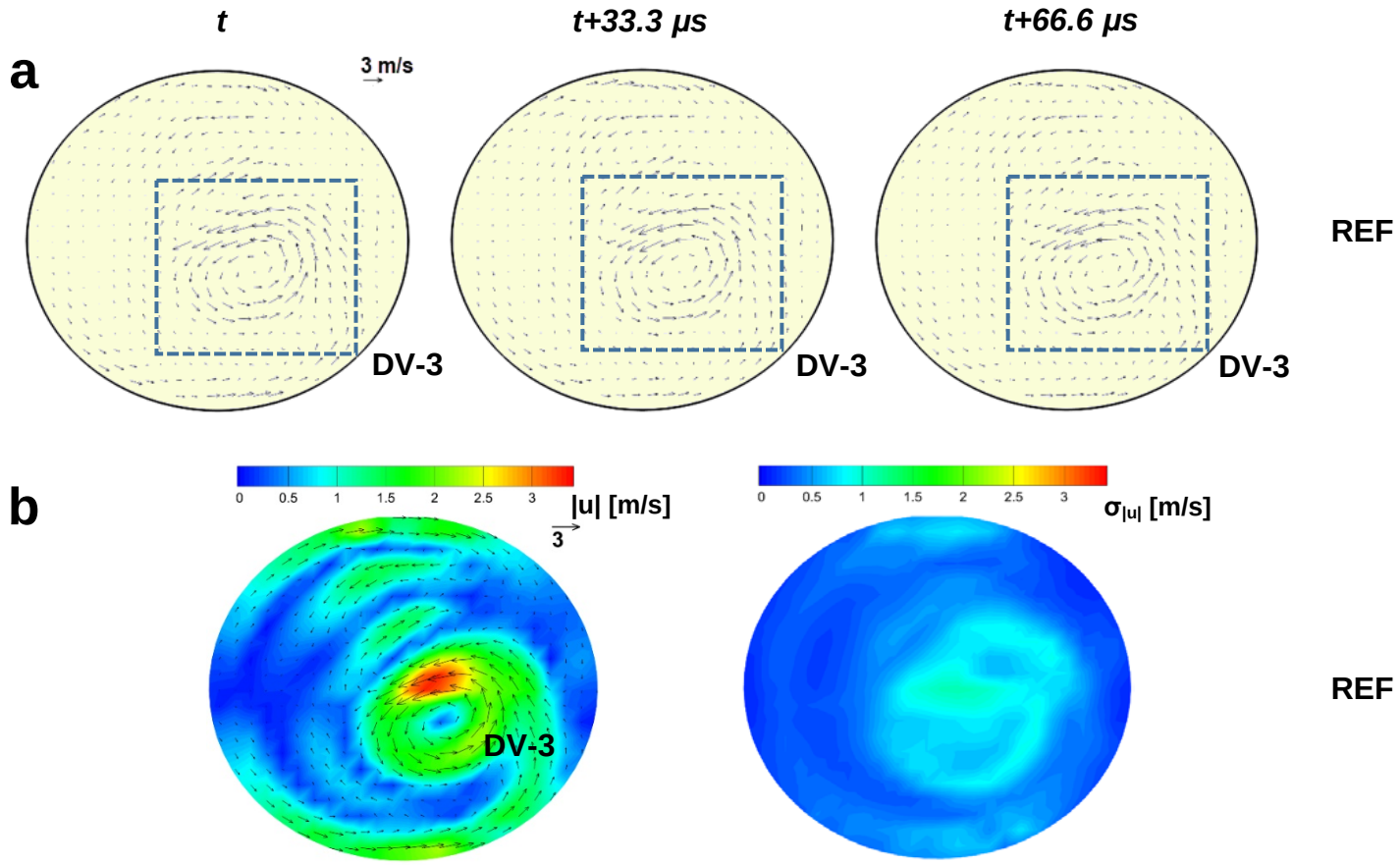

Fig. 7. (a) Sequence of consecutive time instances illustrating a steady secondary-flow field at the apex of the 180^o bend (reference oil at Re=1385/De=631). (b) Velocity-magnitude mean and standard-deviation images for the same flow conditions. The experimental uncertainty $\boldsymbol{U_{\bar{u}}}$ associated with the temporally averaged velocity value is of the order of 0.6% for De=631.

Fig. 8 highlights the quantitative differences in the intensity of the recirculation pattern for the examined samples for the highest Dean number value examined (De=631). Vorticity reduction approximately of the order of 10-18% in all identified regions of interest (DV1-2 and DV3-4 for the upper and lower Dean vortices, as well as SV1-2 for the secondary vortices) is achieved by the OCP liquid compared to reference liquid, as indicated by the relevant contour plots of **Fig. 8a**. On the contrary, the PMA liquid exhibits recirculation of comparable magnitude to the base oil with reference to all identified regions, with the exception of the 'eye' of the lower Dean vortex DV-3, where a reduction approximately equal to 7% is observed. The averaged cross-sectional vorticity magnitude at the tube apex presented in **Fig. 8b** clearly verifies the secondary-flow reducing action of the OCP polymer. Although for the two lower values of the Reynolds number examined the three liquids exhibit comparable magnitude (within the experimental uncertainties) of the overall recirculation pattern, for Re=1385 the OCP sample achieves a measurable vorticity reduction of approximately 14% and 16%, compared to the reference and PMA oils, respectively.

As initially reported by Tsang and James [17], the longitudinal vortical flow setting in besides the primary Poiseuille flow bears resemblance to the vortex pair giving rise to near-wall turbulence. It is

suggested that the suppression of vortical motion in both cases is based on a similar mechanism, i.e. that elastic polymer chains store, and thus extract, energy from the coherent vortices, thus leading to their decay. A similar flow modification mechanism based on elastic-stress gradients and their effect on free shear-layer vorticity has also been described by Kumar and Homsy [45].

On the other hand, the PMA sample consistently exhibits a comparable or even slightly increased cross-sectional vorticity compared to the reference oil for the range of the Reynolds-number values examined. As also suggested by the rheological analysis the specific sample only exhibits shear-thinning characteristics, which have been demonstrated to affect the vortical motion in curved tubes in an enhancing manner [46,47].

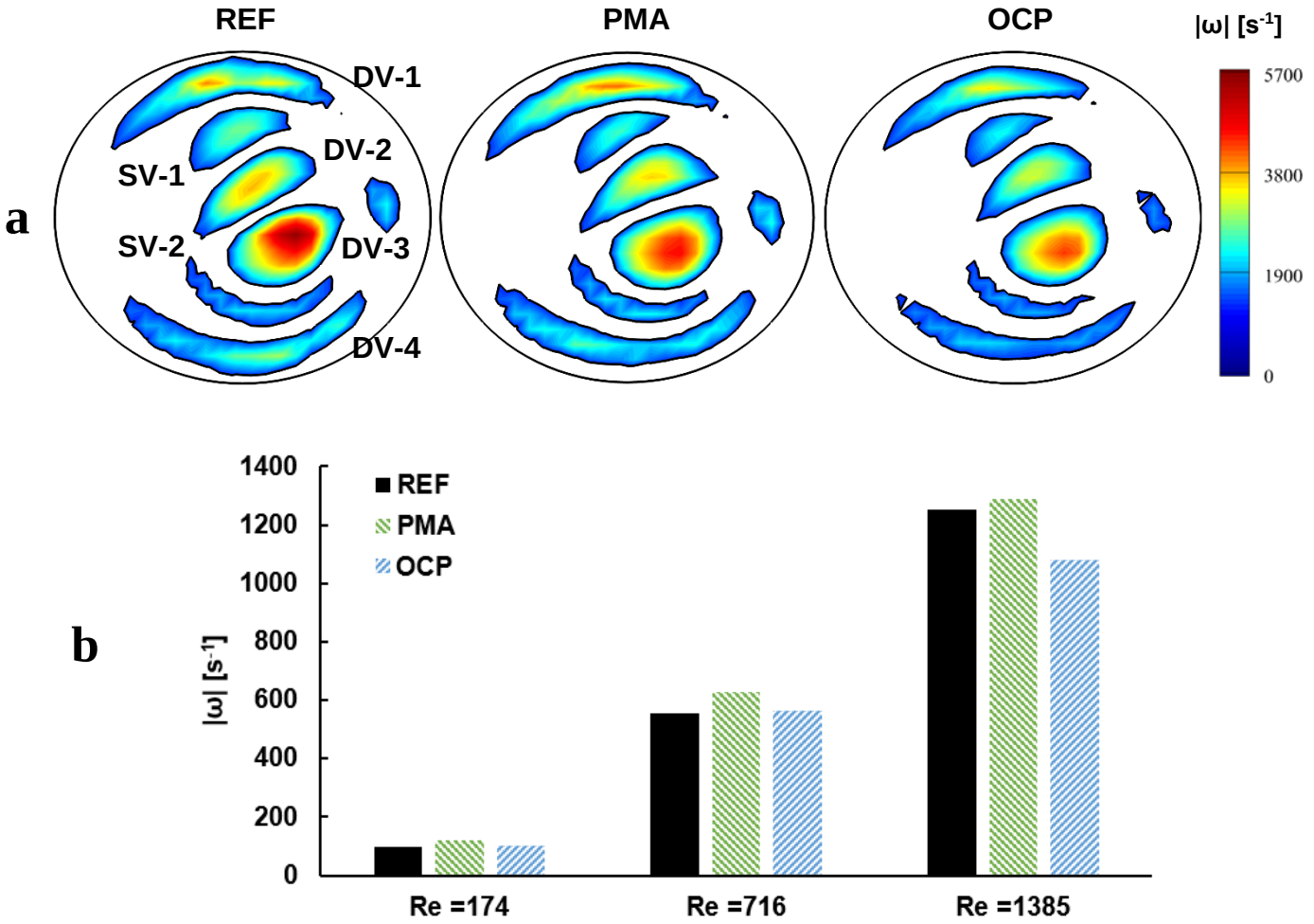

Fig. 8. (a) Average vorticity-magnitude plots highlighting coherent vortical motion at the apex of the 180° bend for the three liquids examined at De=631. Values of vorticity below the contour level of 1300 s^{-1} are cut off. (b) Comparison of spatially-averaged planar vorticity values at the bend apex for the three liquids examined. The uncertainty associated with the spatially averaged values is of the order of 2-3%, with the largest uncertainty corresponding to the lowest Reynolds-number case.

For completeness purposes, the averaged secondary flow field at the outlet of the 180^o-bend for the additised samples is presented in **Fig. 9** for De=631. The effect of the centrifugal force is decreased compared to the apex region and the vorticity of the Dean vortices reduces to less than half of the respective value at the apex. As can been, symmetric pairs of Dean vortices can be observed to occupy

the regions in the vicinity of the tube wall, while no appreciable recirculation pattern appears at the tube core. Besides, no appreciable differences were observed for the three compounds examined.

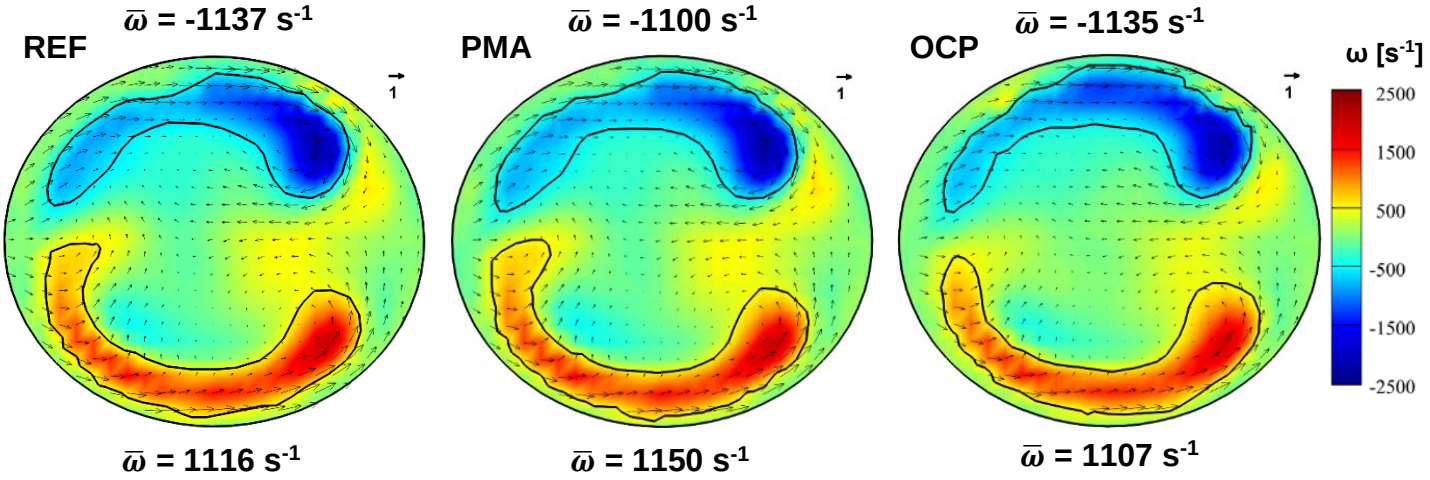

Fig. 9. Velocity vectors over vorticity contour plots depicting the time-averaged secondary-flow field at the outlet of the 180° bend at De=631. No appreciable differences can be detected between the three samples.

The flow efficiency of the hydraulic liquids has been subsequently evaluated in the optical part replicating a typical valve of the hydraulic circuit of an earth-moving machine. **Fig. 10a** presents the averaged velocity field in the centre-plane of the optical part for the highest flow rate examined corresponding to Re=308, based on the hydraulic diameter of the chamber upstream the constriction. As can be seen, high velocities, up to 10 m/s for a flow rate of 20 lpm, set in on the left-hand side of the flow path whereas the liquid under the direct influence of the inlet blockage is almost stagnant. Different regions of recirculation can be detected, namely flow separation due to stagnation at the location of geometry contraction, flow separation at the left-hand-side wall downstream the contraction and a low intensity, shear-driven vortex at the right hand-side of the cross-section upstream the contraction. A liquid mixing or shear layer, i.e. a layer where the high-velocity flow stream interacts with the stagnant fluid, also exists approximately at the symmetry line of the flow path. The standard deviation of the velocity field depicted in **Fig. 10b** makes evident that there are transient flow features, especially in the shear-layer region (mid-cross section of the channel), yet there does not appear to be significant variation in the regions of vortical flow.

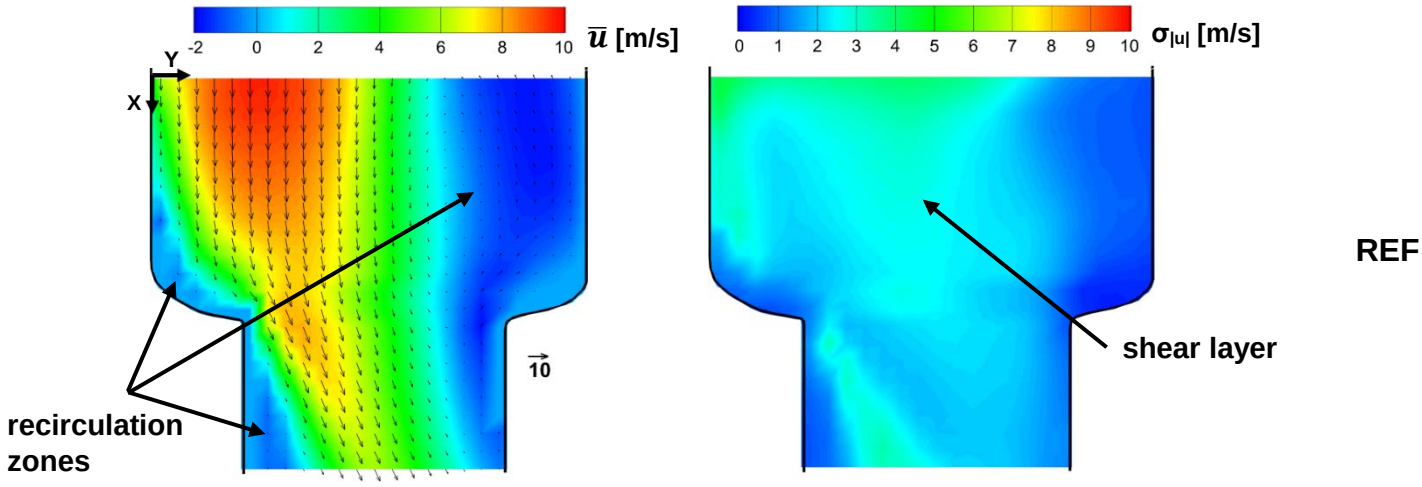

Fig. 10. Average and standard-deviation images of the velocity field at the contraction region of the control-valve replica (reference liquid, Re=308). The experimental uncertainty $\boldsymbol{U_{\bar{u}}}$ associated with the temporally averaged velocity value is of the order of 0.6%

Fig. 11 depicts the cross-flow velocity profiles of the liquids examined at an indicative location of 6.5 mm upstream the contraction, as indicated by the inset of the figure. The thickness of the shear (or mixing) layer δ can be defined as the distance between the locations of zero (i.e. stagnant liquid) and $0.99u_{max}$ velocities. As can be seen, the velocity profiles become less steep and the thickness δ is decreased in the additised oils compared to the reference liquid. Hence, the presence of additives seems to decrease the extent of mixing of the high-velocity fluid stream with the almost stagnant liquid, an indication that hydraulic losses are reduced in such kinds of flow configurations. Diffusion of the mixing layer is induced by small-scale vortices and therefore it is postulated that, once again, elastic stresses tend to inhibit the vortex roll-up process leading to the widening of the buffer region between the two liquid streams. The DNS study of Kumar and Homsy [45] referring to vortex roll-up instabilities in free-shear layers has demonstrated the conceptual mechanism through which polymers reduce flow instabilities, as their simulations revealed flattened shear-layer vortices for non-Newtonian fluids compared to Newtonian counterparts. As demonstrated by **Fig. 11b**, the non-Newtonian samples exhibit a consistent behaviour in the entire upstream region, as for all examined locations the PMA sample exhibits a reduction of the order of 5-7%, while the reduction induced by the OCP polymer is slightly larger and lying in the range 7-8%.

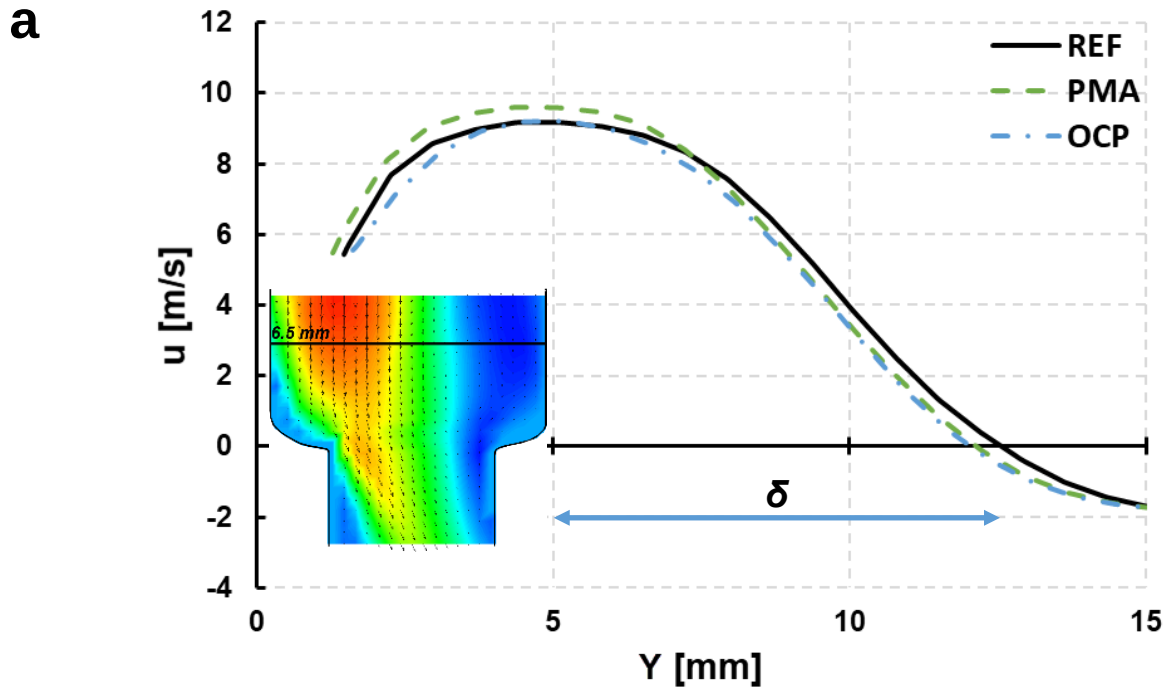

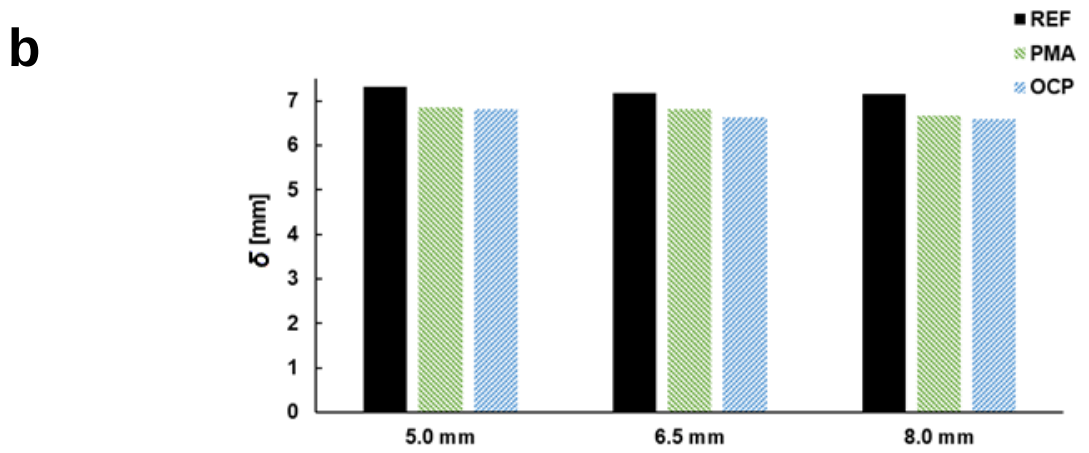

Fig. 11. (a) Cross-flow velocity distribution 6.5 mm upstream the constriction demonstrating the existing shear layer and (b) shear-layer thickness δ at different locations upstream the geometrical constriction of the valve-replica layout for Re=308. The maximum uncertainty in the δ values, designated by the spatial resolution, is equal to 0.4%.

The perturbation-suppressing action of the polymers is further reinforced by **Fig. 12** showing the root mean square (rms) of the u- (**Fig. 12a**) and v-velocity (**Fig. 12b**) components variation in a location (refer to the inset of **Fig. 12b)**, where velocity field instabilities can be detected (also refer to **Fig. 10**). As clearly made evident by **Fig. 12a** referring to the u-component, u_{rms} is reduced under the presence of polymers especially in the region 8mm<X<10mm, i.e. exactly at the location of the geometrical constriction. Besides, the OCP sample also retains lower u_{rms} values compared to base liquid in the entire upstream section (X<8 mm). The inset of **Fig. 12a** presents the respective contour plot of u_{rms} (indicatively for the reference liquid), which makes clear that flow perturbations are non-negligible in the shear-layer region and additive influence is measurable there. **Fig. 12b** illustrates that a similar pattern is observed for the v-component as well, yet much less pronounced, since the v-velocity magnitude is significantly lower compared to the axial velocity u in the duct core. Nevertheless, similar to u_{rms}, the OCP sample suppresses the v-component temporal variations in the entire upstream part.

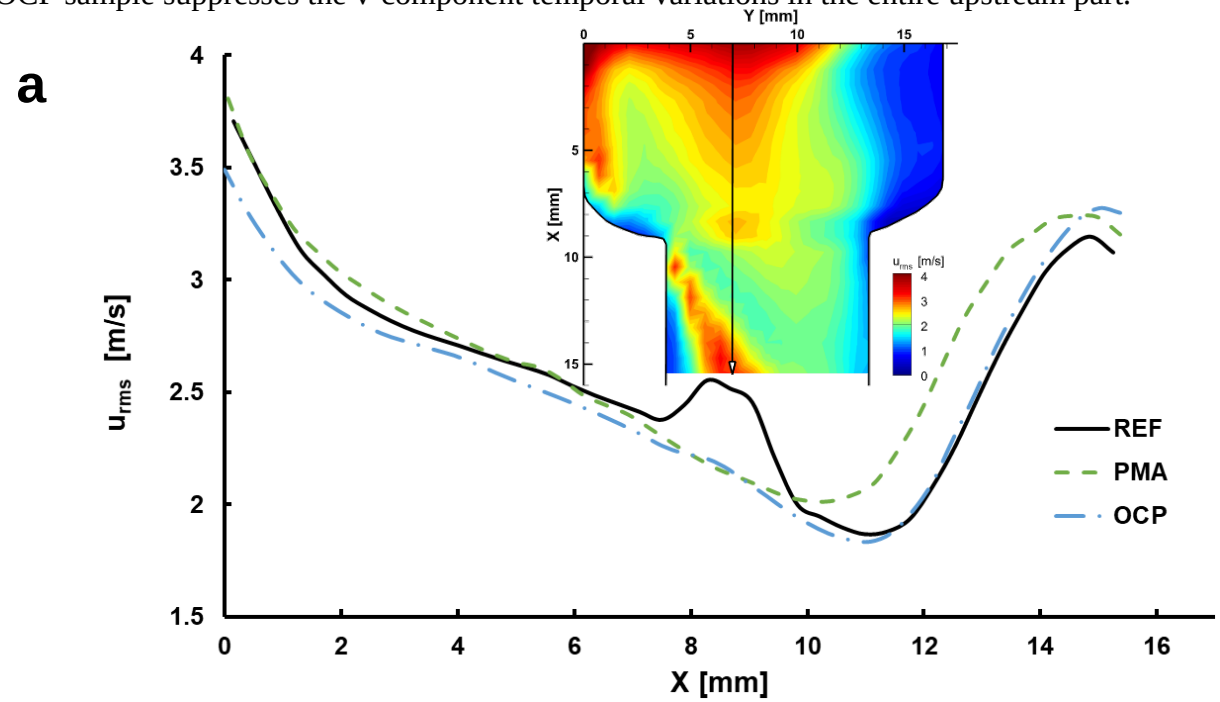

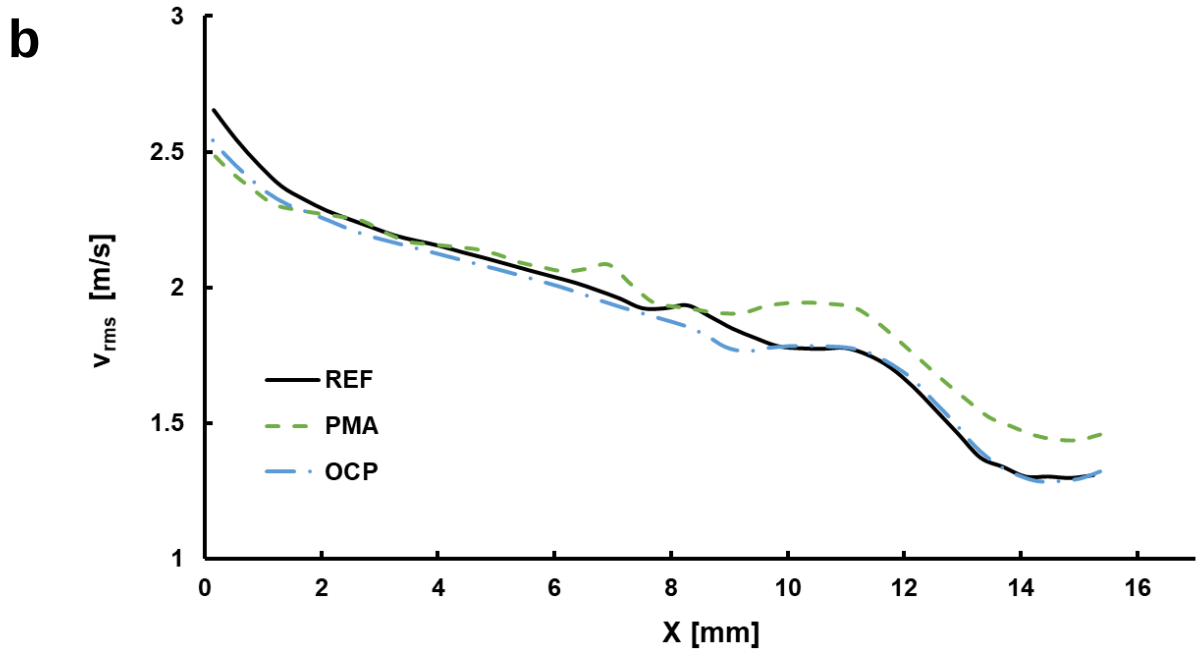

Fig. 12 Velocity rms at the geometrical constriction of the valve-replica for Re=308 illustrating the level of flow perturbations in the shear layer: (a) u-component, (b) v-component. The distributions are extracted on a line corresponding to Y=7mm according to the co-ordinate system of the inset in **Fig. 12a**.

In order to judge on the additive influence on cross-flow vortical motion, **Fig. 13a-c** depict vorticity contours over vector plots at the visualisation plane of the valve optical part for the examined range of Reynolds numbers. An initial observation that can be made is that a coherent corner vortex (CV) forms for Re≥156 in the vicinity of the left boundary layer due to the flow stagnation on the contracting geometry. It is interesting to notice that the CV maximum vorticity is obtained for Re=156, while on the contrary, it reduces for Re=308. This counterintuitive trend is attributed to a 2D to 3D transition of the separating flow, which has been numerically and experimental verified [6,48] in abruptly-contracting geometries under laminar flow conditions. Furthermore, it must be noted that the high vorticity values evident exactly at the location of constriction (**Fig. 13c**) are not associated with vortical motion. An additional shear layer forms due to the steep velocity gradient between the high-velocity stream that changes direction due to its impingement in the contracting wall and the separated flow in the near-wall region. **Fig. 13** presenting the averaged vorticity of the corner vortex elucidates that the additised liquids overall tend to suppress the recirculation intensity compared to the base oil. The maximum decrease achieved by the OCP compound is approximately equal to 38% compared to the base liquid for Re=156, while the respective decrease is around 19% for Re=308. The PMA sample achieves a decrease of 20% for Re=156 yet it exhibits comparable recirculation intensity with the reference fluid for the highest Re value. Findings on the suppression of cross-flow vortices by viscoelastic additives have also been reported in the PIV and DNS studies performed by Tsukahara and Kawaguchi [49,50]. It has been demonstrated that viscoelastic stresses extract energy from the vortices leading to their decay; a conclusion that has been found to stand both in a contracting turbulent flow and in a Rankine vortex superimposed to a laminar Couette flow.

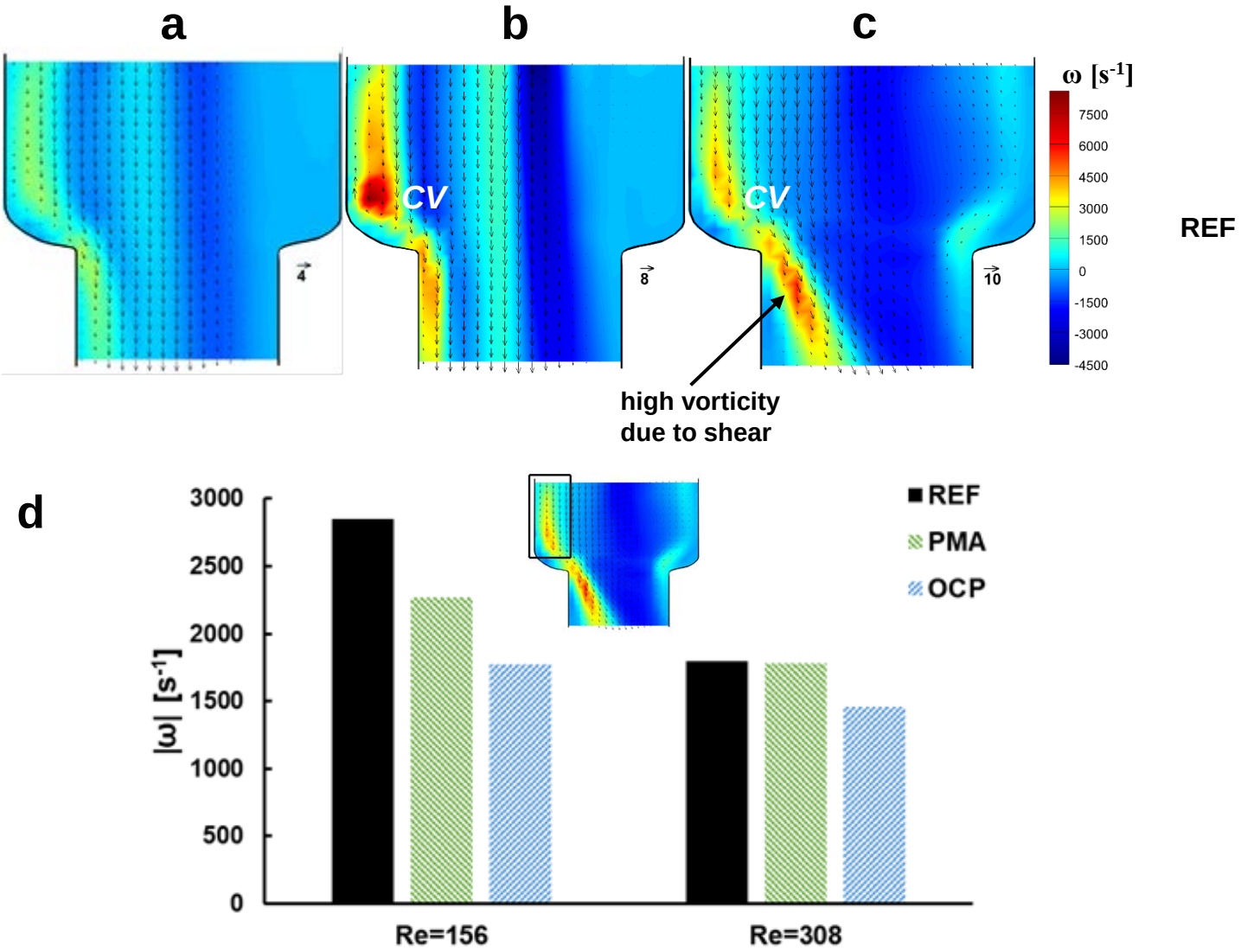

Fig. 13. Time-averaged velocity vectors over vorticity contour plots illustrating the recirculation pattern at the geometrical constriction of the valve-replica for the reference liquid: (a) Re=76, (b) Re=156 and (c) Re=308. The experimental uncertainty $\boldsymbol{U}_{\bar{\omega}}$ lies in the range 0.6-1.0%. (d) Comparison of spatially-averaged planar vorticity values at the constriction location for the three liquids examined. The vorticity values are averaged in the window shown in the inset of the figure, while the uncertainty associated with the spatially averaged values is of the order of 4%, slightly higher compared to the respective for the bend layout due to the reduced dimensions of the sampling window and, thus, number of averaging points.

The effects of polymer rheology on the flow behaviour of the additised samples can be further elucidated by the temporally averaged shear-rates, depicted in **Fig. 14**, in conjunction to the rheological analysis presented in the previous section. The values of the shear rates $\dot{\gamma}$ arising in the examined flow layouts designate the magnitude of the Weissenberg number, normal stress differences (N_1 and N_2) and polymer-solution viscosity reduction, which, in turn, are representative of viscoelastic and shear-thinning effects, respectively. An initial observation that can be made is that the presence of OCP additives reduces the overall extent of high-shear regions associated with vortical motion in both the bend (vortex pairs DV and SV in **Fig. 14a**) and valve flow layouts (cross-flow vortex CV in **Fig. 14b**) compared to reference and PMA liquids.

According to the stability-theory analysis presented in [51] for Couette-flow, considerable effect of elastic forces tends to destabilise the flow, giving rise to vortical motion, while, on the contrary, even small negative values of the second normal stress difference have a stabilising influence. Hence, the fact that the OCP polymer tends to suppress the recirculation pattern in both configurations infers that it is weakly viscoelastic (moderate values of N_1). Indeed, for the shear rates (~10^3 s^{-1}) prevailing in the recirculation regions of the two flow layouts the first normal stress difference values are N_1~10^{-1}. Besides, the ratio of elastic to viscous forces, i.e. the Weissenberg number $Wi = \lambda_H \dot{\gamma}$, is much lower than unity (λ_H~10^{-6} s), hence viscous seem to be dominant over elastic forces. As also reported in the rheological analysis, the limiting value of ξ=0.02 providing a good fit of the viscosity experimental data by the PTT model results to N_2/N_1=-0.01. This value is in agreement with the observations of Denn and Roisman [52] that all viscoelastic liquids employed in their experimental study, which delayed flow instability onset in rotational (Couette) flow where characterised by negative N_2/N_1 values within the range 0.01-0.048. Even an extremely small N_2 value can have a considerable effect on flow instabilities, as, according to stability theory, its contribution is accentuated by a factor depending on the characteristic geometry and eddy length scales [52].

An additional observation that can be made through **Fig. 13** is that effects of shear-thinning should not be considerable for both PMA and OCP in the recirculation regions of the two flow-layouts examined. As shown in the supplementary table of the figure, the maximum shear-rate magnitude recorded is approximately equal to $4 \cdot 10^3$ s^{-1}, whereas, as demonstrated in **Fig. 4**, the non-Newtonian liquids exhibit considerable reduction in their viscosity for shear rates equal or above of 10^5 s^{-1}. Hence, the non-Newtonian nature of the PMA liquid is weak within the examined flow paths and the similar behaviour to the Newtonian liquid is justified. Of course, some re-arrangement of vorticity in the visualised planes is observed, as liquid shear thinning is expected to be more significant in the wall boundary layer or in parts of the manifolds, especially of the valve-replica part, where higher shear-rates arise. The moderate influence of shear-thinning potentially leads to different manifestations of flow instabilities causing slight variations of the obtained flow fields, nevertheless macroscopic after-effects must be negligible.

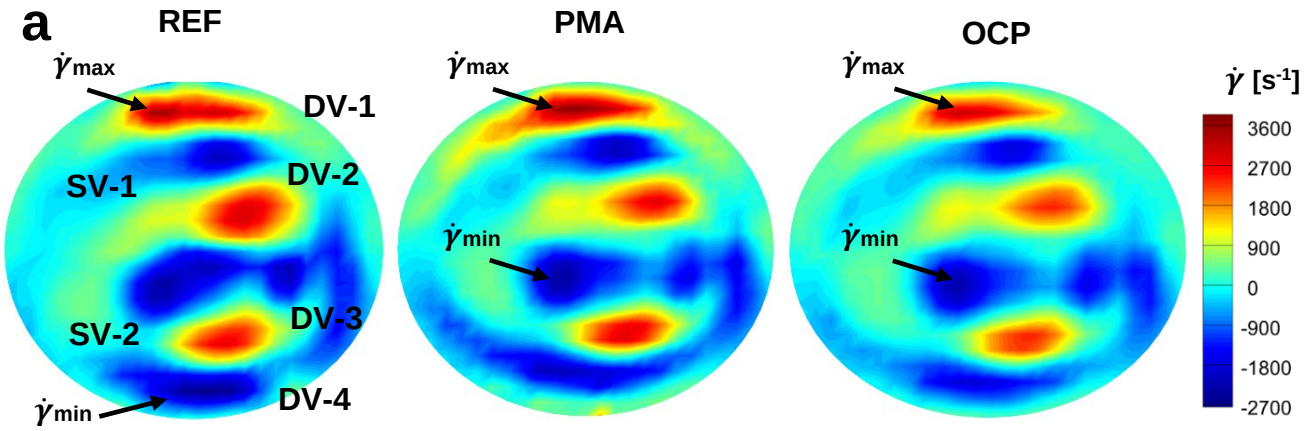

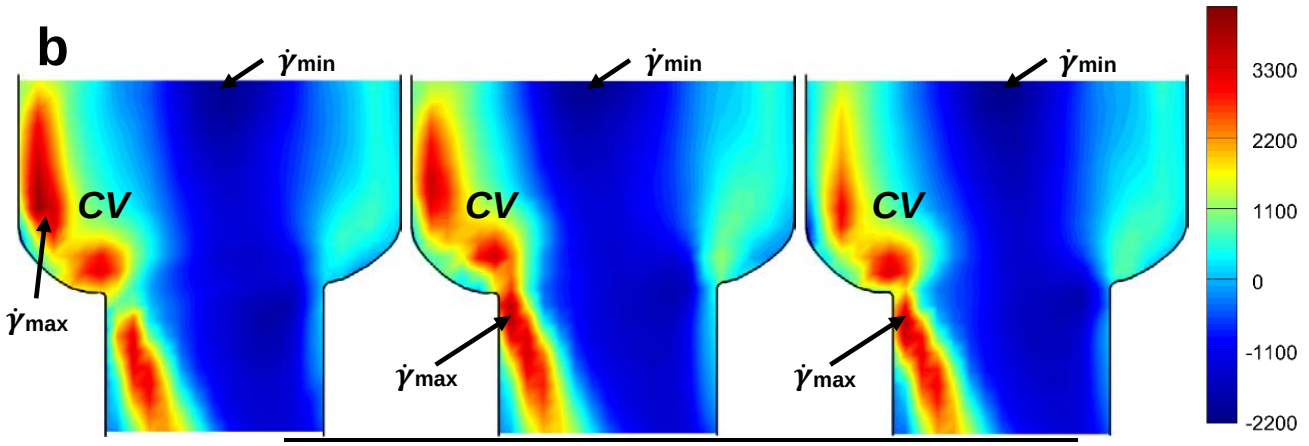

Sample	$\dot{\gamma}_{bend}$ [s^{-1}]	$\dot{\gamma}_{valve}$ [s^{-1}]
REF	[-2674, 3497]	[-2038, 4083]
PMA	[-2400, 3755]	[-2285, 4028]
OCP	[-2369, 3146]	[-2167, 3753]

Fig. 14. Contour plots of the temporally-averaged shear rate $\dot{\gamma}$ in the examined geometries to illustrate the effect of liquid rheology on the arising secondary-flow pattern: (a) 180° bend (Re=1385/De=631) and (b) control-valve replica (Re=308). A table summarising the shear-rate range in each configuration is also included in the figure.

From the industry standpoint, the flow efficiency of hydraulic liquids is evaluated in terms of overall friction losses induced throughout the piping and components, which are eventually reflected in the fuel consumption of the earth-moving machine. The total pressure drop induced by the examined liquids in the section of the hydraulic loop comprising the upstream/downstream manifolds and the optical part for different values of the Reynolds number is shown in **Fig. 15**. The actual manifold/part assembly in each case is also depicted as an inset along with basic dimensions for the bend (**Fig. 15a**) and valve (**Fig. 15b**) parts, respectively. Hence, it must be emphasised that the overall pressure-drop values reflect the combined effect of the friction losses in the straight steel pipes, as well as the losses induced by stagnation and secondary flow in the optical part, with the largest contribution being attributed to the manifolds due to their extended flow path and geometrical complexity.

As illustrated by **Fig. 15**, the OCP liquid exhibits a pressure drop reduction compared to reference in both layouts examined. The reduction, referring to bend and valve models, respectively, is of the order of 11% and 18% for the highest values of the Reynolds examined, which are closer to the operating conditions of the liquids in an actual hydraulic circuit. It is essential to note that the pressure drop estimation directly from the pressure-sensor values is associated with high uncertainty, of the order of 8% even for the high Δp values obtained. More accurate measurements can be obtained either by considerably increasing the total length of the flow loop or through a high-accuracy differential pressure transducer. Notwithstanding these facts, especially the values of **Fig. 15b** constitute a strong indication of pressure-drop reduction by the OCP sample compared to reference. The enhanced flow efficiency of the OCP liquid is justifiable by the suppression of the recirculation pattern and mixing layers arising in the flow paths and possibly facilitated by shear-thinning effects. Pressure-drop suppression is more pronounced in the valve flow path due to the complexity of the manifold, where coherent recirculation patterns and flow stagnation are also expected to set in, thus giving ground to more extensive polymer action. On the contrary, the pressure loss induced by the flow of the PMA liquid seem comparable to reference for both layouts, indicating once again the weak non-Newtonian nature of the polymeric solution under the specific flow conditions.

4. Conclusions

The present study comprises a rheological analysis and PIV measurements of two oil-based, non-Newtonian liquids (PMA and OCP) suitable to serve as working media for the hydraulic circuit of typical earth-moving machines. Precursor viscosity variation with shear rate measurements, verifying the shear-thinning nature of both liquids examined, also served as validation for the FENE model, which, in a second step, verified that the OCP polymer forms flexible chains within the liquid matrix. On the contrary, FENE failed to predict the viscosity variation of the PMA sample, which is indicative of rigid polymeric chains, not possible to exist in an entangled state. Furthermore, the PTT model was found to provide a good fit for the experimentally-measured viscosity data for values of the affinity parameter ξ up to 0.02, leading to a small negative value of the second normal stress difference.

PIV conducted in optical replicas of typical components located in the hydraulic circuit of heavy-duty machines reflected the differences observed in the rheology of the non-Newtonian liquids. The general conclusion that could be established for both configurations examined, i.e. an 180^o bend and a geometrical constriction, is that the OCP liquid exhibits enhanced performance compared to the reference monograde oil, in terms of secondary-flow magnitude, perturbation and mixing layer suppression. The combined after-effect of the polymer action resulted in a measurable reduction of pressure drop for flow conditions similar to those prevailing in the actual industrial application, despite the limited flow-path of the hydraulic circuits employed. On the contrary, the PMA liquid, for which an elastic behaviour could not be verified, showed comparable behaviour to the base oil with reference to recirculation-pattern magnitude and induced pressure drop. Shear-thinning effects were found to be very weak for both non-Newtonian liquids in mention for the shear-rates measured in the recirculation regions of the examined flow layouts. They are expected to only have a minor effect on the manifestation of possible boundary layer instabilities in parts of the loop upstream of the visualised cross-sections. Overall, the study has demonstrated the strong influence of liquid rheology on the dynamic flow behaviour of dilute polymer solutions. From an industrial standpoint, it has demonstrated the suitability of the OCP polymer for the enhancement of the flow efficiency of highly viscous liquids.

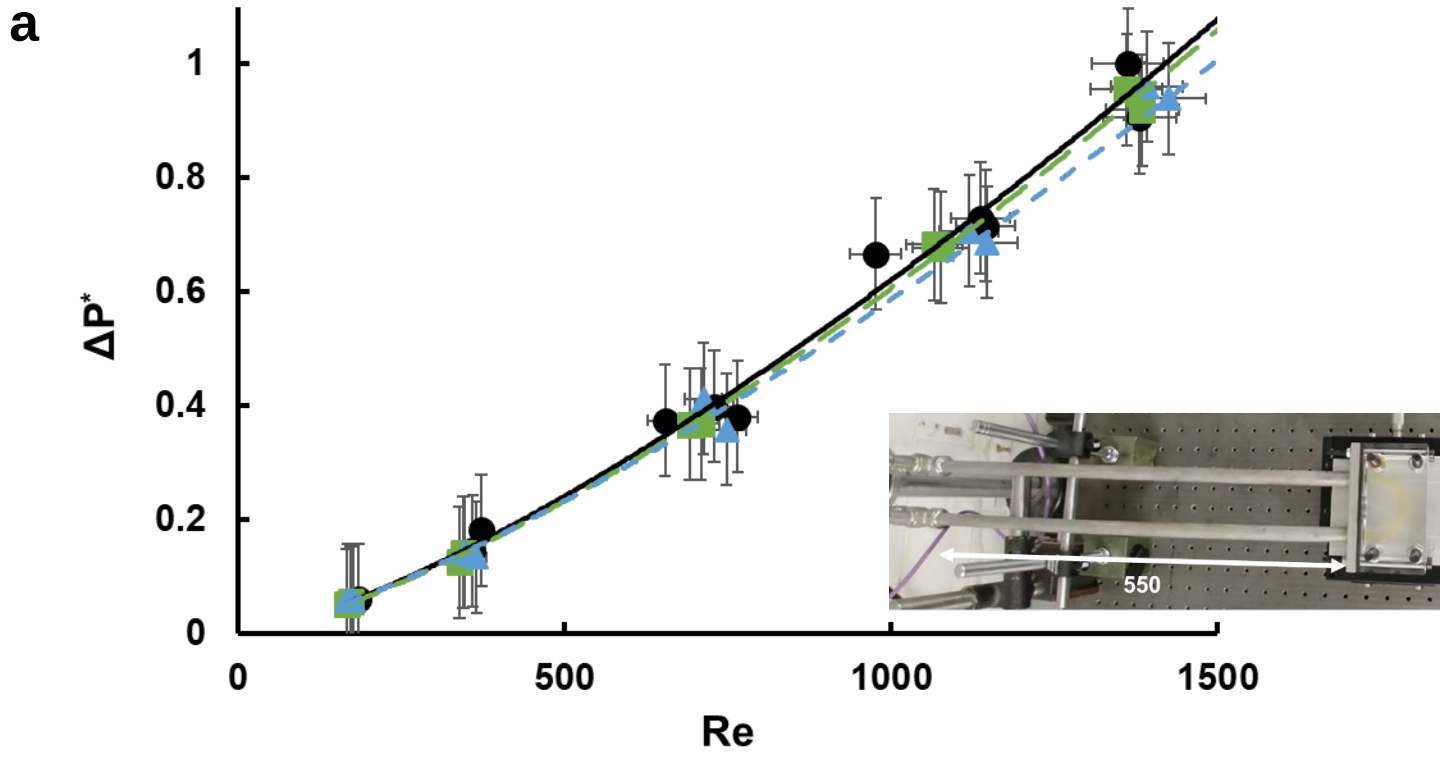

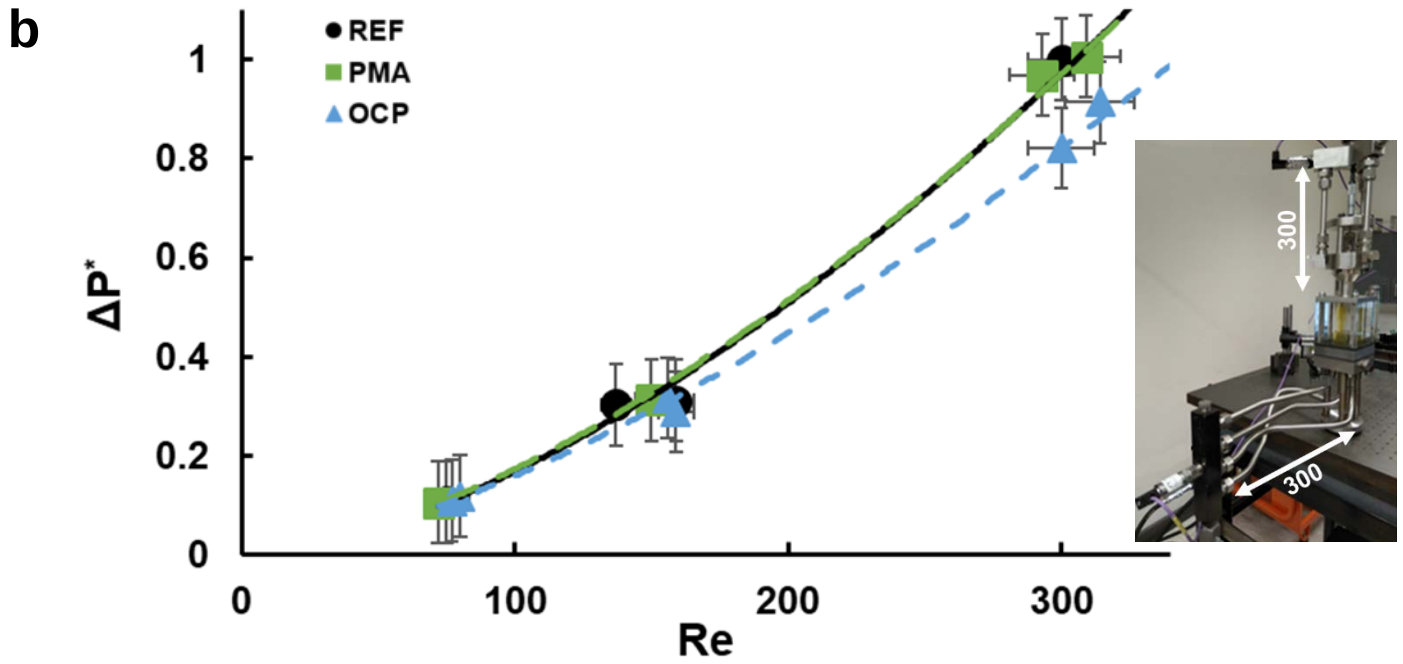

Fig. 15. Dimensionless pressure drop ($\Delta p^{*}=\Delta p/\Delta p_{max}$) in the flow path realised by the manifolds and the optical part as a function of Re for different oil samples: (a) 180^{o} bend and (b) valve replica. Δp_{max} is equal to 2.5bar and 3.0bar in the bend and valve models respectively. Insets depict the manifold/part assembly in each case along with basic dimensions. Each experimental point corresponds to the average of at least 50 pressure-sensor recordings. Experimental data have been fitted with curves produced by power-law functions (R^2>0.99 in all cases) to demonstrate the trend of pressure drop with Re.

Acknowledgments

This work has received funding from the Lubrizol Corporation. The authors declare no competing financial interest.

References

[1] K. Holmberg, A. Erdemir, Influence of tribology on global energy consumption, costs and emissions, Friction. 5 (2017) 263–284. doi:10.1007/s40544-017-0183-5.

[2] J.D. Zimmerman, M. Pelosi, C.A. Williamson, M. Ivantysynova, Energy consumption of an LS excavator hydraulic system, in: 2007 ASME Int. Mech. Eng. Congr. Expo., 2007.

[3] M. Rowe, Measurements and computations of flow in pipe bends, J. Fluid Mech. 43 (1970) 771–783.

[4] A. Kalpakli Vester, R. Örlü, P.H. Alfredsson, Turbulent Flows in Curved Pipes: Recent Advances in Experiments and Simulations, Appl. Mech. Rev. 68 (2016) 050802. doi:10.1115/1.4034135.

[5] S.C.R. Dennis, A.T. Smith, Steady flow through a channel with a symmetrical Steady flow through in the form of a step constriction, 372 (1980) 393–414.

[6] H. Stüer, A. Gyr, W. Kinzelbach, Laminar separation on a forward facing step Edited by Foxit Reader, Eur. J. Mech. - B/Fluids. 18 (2008) 675–692.

[7] C.M. White, M.G. Mungal, Mechanics and Prediction of Turbulent Drag Reduction with Polymer Additives, Annu. Rev. Fluid Mech. 40 (2008) 235–256. doi:10.1146/annurev.fluid.40.111406.102156.

[8] T. Min, H. Choi, J.Y. Yoo, Maximum drag reduction in a turbulent channel flow by polymer additives, J. Fluid Mech. 486 (2003) 91–109. doi:10.1017/S0022112003005597.

[9] Y. Dubief, C.M. White, V.E. Terrapon, E.S.G. Shaqfeh, P. Moin, S.K. Lele, On the coherent drag-reducing and turbulence-enhancing behaviour of polymers in wall flows, J. Fluid Mech. 514 (2004) 271–280. doi:10.1017/S0022112004000291.

[10] R. Sureshkumar, A.N. Beris, R.A. Handler, Direct numerical simulation of the turbulent channel flow of a polymer solution, Phys. Fluids. 9 (1997) 743–755. doi:10.1063/1.869229.

[11] A.S. Pereira, G. Mompean, L. Thais, E.J. Soares, Transient aspects of drag reducing plane Couette flows, J. Nonnewton. Fluid Mech. 241 (2017) 60–69. doi:10.1016/j.jnnfm.2017.01.008.

[12] N. Burshtein, K. Zografos, A.Q. Shen, R.J. Poole, S.J. Haward, Inertioelastic flow instability at a stagnation point, Phys. Rev. X. 7 (2017) 1–18. doi:10.1103/PhysRevX.7.041039.

[13] C.D. Dimitropoulos, R. Sureshkumar, A.N. Beris, Direct numerical simulation of viscoelastic turbulent channel flow exhibiting drag reduction: Effect of the variation of rheological parameters, J. Nonnewton. Fluid Mech. 79 (1998) 433–468. doi:10.1016/S0377-0257(98)00115-3.

[14] F.J.H. Gijsen, E. Allanic, F.N. Van De Vosse, J.D. Janssen, The influence of the non-Newtonian properties of blood on the flow in large arteries: Unsteady flow in a 90°curved tube, J. Biomech. 32 (1999) 705–713. doi:10.1016/S0021-9290(99)00014-7.

[15] E.M. Cherry, J.K. Eaton, Shear thinning effects on blood flow in straight and curved tubes, Phys. Fluids. 25 (2013). doi:10.1063/1.4816369.

[16] W.M. Jones, O.H. Davies, The flow of dilute aqueous solutions of macromolecules in various geometries. II. Straight pipes of circular cross-section, J. Phys. D. Appl. Phys. 9 (1976) 735–752. doi:10.1088/0022-3727/9/5/007.

[17] H.Y. Tsang, D.F. James, Reduction of Secondary Motion in Curved Tubes by Polymer Additives, J. Rheol. (N. Y. N. Y). 24 (1980) 589–601. doi:10.1122/1.549574.

[18] T.A. Pimenta, J.B.L.M. Campos, Friction losses of Newtonian and non-Newtonian fluids flowing in laminar regime in a helical coil, Exp. Therm. Fluid Sci. 36 (2012) 194–204. doi:10.1016/j.expthermflusci.2011.09.013.

[19] L. Helin, L. Thais, G. Mompean, Numerical simulation of viscoelastic Dean vortices in a curved duct, J. Nonnewton. Fluid Mech. 156 (2009) 84–94. doi:10.1016/j.jnnfm.2008.07.002.

[20] J. Malheiro, P.J. Oliveira, F.T. Pinho, Parametric study on the three-dimensional distribution of velocity of a FENE-CR fluid flow through a curved channel, J. Nonnewton. Fluid Mech. 200 (2013) 88–102. doi:10.1016/j.jnnfm.2012.12.007.

[21] S. Chono, Y. Iemoto, Numerical simulation of viscoelastic flow in two-dimensional L-shaped channels, J. Rheol. 36 (1992) 335–356. doi:10.1122/1.550369.

[22] M.Y. Hwang, H. Mohammadigoushki, S.J. Muller, Flow of viscoelastic fluids around a sharp microfluidic bend: Role of wormlike micellar structure, Phys. Rev. Fluids. 2 (2017) 043303. doi:10.1103/PhysRevFluids.2.043303.

[23] Y. Zhang, H. Mohammadigoushki, M.Y. Hwang, S.J. Muller, Flow of wormlike micellar fluids around a sharp bend: Effects of branching and shear-banding, Phys. Rev. Fluids. 3 (2018) 1–13. doi:10.1103/PhysRevFluids.3.093301.

[24] J. Zilz, R.J. Poole, M.A. Alves, D. Bartolo, B. Levaché, A. Lindner, Geometric scaling of a purely elastic flow instability in serpentine channels, J. Fluid Mech. 712 (2012) 203–218. doi:10.1017/jfm.2012.411.

[25] R.J. Poole, A. Lindner, M.A. Alves, Viscoelastic secondary flows in serpentine channels, J. Nonnewton. Fluid Mech. 201 (2013) 10–16. doi:10.1016/j.jnnfm.2013.07.001.

[26] Y. Fan, R.I. Tanner, N. Phan-Thien, Fully developed viscous and viscoelastic flows in curved pipes, J. Fluid Mech. 440 (2001) 327–357. doi:10.1017/S0022112001004785.

[27] M. Norouzi, M.H. Kayhani, C. Shu, M.R.H. Nobari, Flow of second-order fluid in a curved duct with square cross-section, J. Nonnewton. Fluid Mech. 165 (2010) 323–339. doi:10.1016/j.jnnfm.2010.01.007.

[28] P. Saramito, J.M. Piau, Flow characteristics of viscoelastic fluids in an abrupt contraction by using numerical modeling, J. Nonnewton. Fluid Mech. 52 (1994) 263–288. doi:10.1016/0377-0257(94)80055-3.

[29] M.A. Alves, F.T. Pinho, P.J. Oliveira, Viscoelastic flow in a 3D square/square contraction: Visualizations and simulations, J. Rheol. 52 (2008) 1347–1368. doi:10.1122/1.2982514.

[30] D.B. Pitz, A.T. Franco, C.O.R. Negrão, Effect of the Reynolds number on viscoelastic fluid flows through axisymmetric sudden contraction, J. Brazilian Soc. Mech. Sci. Eng. 39 (2017) 1709–1720. doi:10.1007/s40430-017-0719-7.

[31] R.J. Poole, M.P. Escudier, A. Afonso, F.T. Pinho, Laminar flow of a viscoelastic shear-thinning liquid over a backward-facing step preceded by a gradual contraction, Phys. Fluids. 19 (2007) 1–17. doi:10.1063/1.2769380.

[32] M. Rubinstein, R.H. Colby, Polymer Physics, Oxford University Press, 2003.

[33] P.C. Sousa, E.J. Vega, R.G. Sousa, J.M. Montanero, M.A. Alves, Measurement of relaxation times in extensional flow of weakly viscoelastic polymer solutions, Rheol. Acta. 56 (2017) 11–20. doi:10.1007/s00397-016-0980-1.

[34] W. Thielicke, E.J. Stamhuis, PIVlab – Towards User-friendly, Affordable and Accurate Digital Particle Image Velocimetry in MATLAB, J. Open Res. Softw. 2 (2014). doi:10.5334/jors.bl.

[35] R.J. Moffat, Describing the uncertainties in experimental results, Exp. Therm. Fluid Sci. 1 (1988) 3–17. doi:10.1016/0894-1777(88)90043-X.

[36] A. Sciacchitano, B. Wieneke, PIV uncertainty propagation, Meas. Sci. Technol. 27 (2016). doi:10.1088/0957-0233/27/8/084006.

[37] B. Wieneke, PIV uncertainty quantification from correlation statistics, Meas. Sci. Technol. 26 (2015) 074002. doi:10.1088/0957-0233/26/7/074002.

[38] B. Bird, C.F. Curtiss, R.C. Armstrong, O. Hassager, Dynamics of Polymeric Liquids: Kinetic Theory, 2nd ed., Wiley-Interscience, 1987.

[39] M. Herrchen, H.C. Ottinger, A detailed comparison of various FENE dumbbell models, J. Nonnewton. Fluid Mech. 68 (1997) 17–42.

[40] S. Xue, N. Phan-Thien, R.I. Tanner, Numerical study of secondary flows of viscoelastic fluid in straight pipes by an implicit finite volume method, J. Nonnewton. Fluid Mech. 59 (1995) 191–213.

[41] J.J. Magda, C.-S. Lee, S.J. Muller, R.G. Larson, Rheology, Flow Instabilities, and Shear-Induced Diffusion in Polystyrene Solutions, Macromolecules. (1993) 1696–1706.

[42] I.K. Karathanassis, E. Papanicolaou, V. Belessiotis, G.C. Bergeles, Flow and temperature fields in cooling devices with embedded serpentine tubes, Numer. Heat Transf. Part A Appl. 66 (2014). doi:10.1080/10407782.2014.884864.

[43] D.E. Olson, B. Snyder, The upstream scale of flow development in curved circular pipes, J. Fluid Mech. 150 (1985) 139–158.

[44] K.C. Cheng, F.P. Yuen, Flow Visualization Studies on Secondary Flow Patterns in Straight Tubes Downstream of a 180 deg Bend and in Isothermally Heated Horizontal Tubes, J. Heat Transfer. 109 (2009) 49. doi:10.1115/1.3248066.

[45] S. Kumar, G.M. Homsy, Direct numerical simulation of hydrodynamic instabilities in two- and three-dimensional viscoelastic free shear layers, J. Nonnewton. Fluid Mech. 83 (1999) 249–276.

[46] T. Kluge, A. Kalra, G. Belfort, Viscosity effects on Dean vortex membrane microfiltration, Am. Inst. Chem. Eng. AIChE J. 45 (1999) 1913–1926.

[47] P. Bayat, P. Rezai, Semi-Empirical Estimation of Dean Flow Velocity in Curved Microchannels, Sci. Rep. (2017) 1–13. doi:10.1038/s41598-017-13090-z.

[48] D. Wilhelm, C. Hrtel, L. Kleiser, Computational analysis of the two-dimensionalthree-dimensional transition in forward-facing step flow, J. Fluid Mech. 489 (2003). doi:10.1017/S0022112003004440.

[49] T. Tsukahara, Y. Kawaguchi, Turbulent Flow of Viscoelastic Fluid Through Complicated Geometry, in: J. de Vicente (Ed.), Viscoelasticity From Theory to Biol. Appl., IntechOpen, 2012: pp. 33–58.

[50] T. Tsukahara, M. Motozawa, D. Tsurumi, Y. Kawaguchi, PIV and DNS analyses of viscoelastic turbulent flows behind a rectangular orifice, Int. J. Heat Fluid Flow. 41 (2013) 66–79. doi:10.1016/j.ijheatfluidflow.2013.03.011.

[51] R.F. Ginn, M.. Denn, Rotational Stability in Viscoelastic Liquids: Theory, AIChE J. 15 (1969) 450–454.

[52] M.M. Denn, J.J. Roisman, Rotational Stability and Measurement of Normal Stress Functions in Dilute Polymer Solutions, AIChE J. 15 (1969) 454–459.